

We are IntechOpen, the world's leading publisher of Open Access books Built by scientists, for scientists

6,900

Open access books available

186,000

International authors and editors

200M

Downloads

Our authors are among the

154

Countries delivered to

TOP 1%

most cited scientists

12.2%

Contributors from top 500 universities



WEB OF SCIENCE™

Selection of our books indexed in the Book Citation Index
in Web of Science™ Core Collection (BKCI)

Interested in publishing with us?
Contact book.department@intechopen.com

Numbers displayed above are based on latest data collected.
For more information visit www.intechopen.com



Dyadic Green's Function for Multilayered Planar, Cylindrical, and Spherical Structures with Impedance Boundary Condition

Shiva Hayati Raad and Zahra Atlasbaf

Abstract

The integral equation (IE) method is one of the efficient approaches for solving electromagnetic problems, where dyadic Green's function (DGF) plays an important role as the Kernel of the integrals. In general, a layered medium with planar, cylindrical, or spherical geometry can be used to model different biomedical media such as human skin, body, or head. Therefore, in this chapter, different approaches for the derivation of Green's function for these structures will be introduced. Due to the recent great interest in two-dimensional (2D) materials, the chapter will also discuss the generalization of the technique to the same structures with interfaces made of isotropic and anisotropic surface impedances. To this end, general formulas for the dyadic Green's function of the aforementioned structures are extracted based on the scattering superposition method by considering field and source points in the arbitrary locations. Apparently, by setting the surface conductivity of the interfaces equal to zero, the formulations will turn into the associated problem with dielectric boundaries. This section will also aid in the design of various biomedical devices such as sensors, cloaks, and spectrometers, with improved functionality. Finally, the Purcell factor of a dipole emitter in the presence of the layered structures will be discussed as another biomedical application of the formulation.

Keywords: biomedical, dyadic Green's function, integral equation, 2D materials, sensors, Purcell factor

1. Introduction

Planarly, cylindrically and spherically layered media have been widely used to model the human skin, body, or head. In particular, a rectangular slab is proposed to model and analyze skin temperature distribution [1]. Moreover, in the multilayered skin model, three stacked layers are exploited to simulate the performance of the epidermis, dermis, and sub-cutis parts of the skin [2]. In other research, a planarly layered medium has been proposed as the simplified human body model by considering the impact of skin, fat, and muscle in the electromagnetic performance [3]. Cylindrical-shaped equivalent phantom of the skin is alternatively used to characterize the interactions between an antenna and the human body [4]. For a more precise investigation, multilayered cylinders are proposed to model a biological system with different tissues [5]. Considering spherical geometrics, the interactions of a

three-layered spherical human head model with a finite-length dipole and a cellular phone helical antenna are investigated using Green's function [6, 7]. The research is extended to the six-layered model, including skin, fat, bone, dura, CSF, and brain layers of the head [8]. This model has also been used to explore the impact of the shapes and positions of coils in the MRI system [9]. For the analysis of the aforementioned structures, integral equation (IE) based methods have been widely used. Dyadic Green's function, which is a powerful method to calculate the electromagnetic response for different excitation sources, plays an essential role in the IE method [10–12].

Different mathematical approaches can be utilized to calculate the dyadic Green's function. The dyadic Green's function in a homogeneous environment can be expressed in terms of vector functions M , N , and L . The Green's function is singular when the field and observation points coincide. In this case, Green's function can be written as the main part plus the portion proportional to the impulse function. This type of decomposition of the Green's function is not unique and depends on the shape of the volume that separates the environment [13]. In general, to obtain the dyadic Green's function in a layered medium, the Green's function of the homogeneous environment can be used. Then, the effect of inhomogeneity can be considered by adding reflected and transmitted waves to the dyadic Green's function [14]. In a similar approach, called the scattering superposition method, the scattering Green's function in each layer is expressed in terms of vector wave functions with the unknown coefficients that are obtained by applying the boundary conditions [15]. Moreover, to calculate the Green's function of a medium by impedance method, instead of each dielectric layer a transmission line, and instead of each metallic layer a current source can be considered in the equivalent model in the rectangular, cylindrical, and spherical coordinates [15–17].

Considering medical diagnostics and treatment, planarly, cylindrically and spherically layered media are engineered mainly with plasmonic materials. In this regard, the interaction of an environment with a nanometer-scale dipole emitter is of interest in different biomedical fields. For example, the optical activity of the proteins can be investigated using Green's tensor approach. Furthermore, a single excited molecule in the vicinity of a metallic structure can be potentially used in the sensors because of behaving as a resonant filter. Moreover, the point source is an appropriate model for the concentrated light sources which are used in medical applications [18]. Following these trends, different plasmonic structures have been presented theoretically and realized in the real environment. For example, the effect of the size of the gold nanoparticles on the decay rate and the energy transfer of dipole emitters is investigated using Green's tensor formulation and compared with the results obtained from the fabrication [19]. The same analysis is carried out for a metallic cylinder coated with a dielectric layer and the resulted integrals are solved numerically [20]. Also, Fermat's golden rule is used to connect the imaginary part of the Green's function to the radiation impedance of the dipole antenna adjacent to a medium, and the Purcell factor is extracted for the planar meta-surface, which is then experimentally characterized in the microwave frequency band [21].

Recently, graphene's plasmons are proposed as the low loss and reconfigurable alternative to the plasmons of the noble metals. There are two approaches to use graphene in analytical and numerical methods. In the first one, the graphene boundary is modeled with a 2D surface, characterized by its surface conductivity, whereas in the second one, the graphene layer is replaced by a very thin dielectric [22]. Although the latter can be analyzed using the available formulas previously presented for the multilayered dielectric structures in the literature [13, 23], graphene analysis using surface conductivity model has many advantages. First, in the dielectric model, each graphene interface adds an extra layer to the structure. Therefore, when the number of graphene layers is large, the problem becomes very complicated. Secondly,

in the dielectric model, it is necessary to compute the special functions of the cylindrical and spherical coordinates with complex arguments, which requires the implementation of specific algorithms for their effective calculation [24], while in the impedance boundary condition method, the surface conductivity of graphene appears as a coefficient for special functions. Third, in the dielectric model, the thickness of the graphene layer is considered to be about 0.335 nm, which is often very small compared to other geometrical parameters and makes the convergence of the analytical functions slow [25]. Also, if the goal is using the dielectric model in numerical methods, it is necessary to use a dense mesh for the equivalent dielectric of the graphene that is not optimal in terms of time and memory [26].

Applying the graphene surface conductivity model for the derivation of the Green's function has been considered in recent years. For example, for the graphene sheet under electric bias, the dyadic Green's function is derived by the Hertzian potential and plane-wave expansion methods and the corresponding integrals are solved with the saddle point method [27, 28]. Also, the method is expanded for the analysis of graphene with tensor surface conductivity which can be used to analyze graphene with magnetic bias or spatial dispersion. Romberg's integration procedure is proposed for the numerical solution of the resulting integrals [29]. In another research, the analysis of the electric dipole in the proximity of the parallel plate waveguide with graphene walls is studied by extracting the Green's function and calculating the spontaneous emission. It is found that symmetric and asymmetric plasmonic modes lead to a sharp increase in this parameter [30]. As another instance, a point source is taken into account in the vicinity of the infinite cylinder with graphene cover and it is observed that by changing the distance of the source from the cylinder as well as changing the chemical potential of the graphene layer, the Fano resonances can be controlled [31]. In this chapter, the dyadic Green's function of various planar, cylindrical, and spherical geometries with impedance boundary conditions will be calculated using the scattering superposition method. Specifically, we have focused on the graphene material due to its wide range of applications. Apparently, another 2D material can be considered by replacing the graphene surface conductivity with the surface conductivity of the desired material. The presented formulas can be potentially used to design various biomedical devices. Moreover, by approaching the surface impedance to zero, these structures can be potentially used to investigate the interaction of the human body with different electromagnetic sources. For the Green's function calculation of complex media in different coordinates using vector wave functions, the reader is referred to [32–35].

2. Surface conductivity of graphene material under different conditions

Graphene is a two-dimensional material made of carbon atoms and can be considered in the solution of Maxwell's equations using surface conductivity boundary condition [23]. Depending on the geometrical and optical conditions, graphene surface conductivity can be isotropic or anisotropic. The purpose of this section is to provide an overview of the graphene surface conductivity under different conditions (electric bias, magnetic bias, and spatial dispersion) and for different geometries (continuous or patterned sheets).

It should be noted that graphene material is mainly synthesized through four methods, including 1) mechanical exfoliation of highly ordered pyrolytic graphite (HOPG), 2) the epitaxial growth of graphene on silicon carbide (SiC), 3) the reduction of graphene oxide, and 4) chemical vapor deposition (CVD) technique. The comparison of these methods in terms of quality and the fabricated area is provided in **Table 1** [36].

Method	Quality	Area
Mechanical exfoliation of highly ordered pyrolytic graphite (HOPG)	Very high	Small
Epitaxial growth of graphene on silicon carbide (SiC)	Medium	Large (3–4 inches wafers)
Reduction of graphene oxide (rGO)	Medium	Large
Chemical vapor deposition (CVD)	High	Very large (30 inches)

Table 1.

Comparison of the quality and area of synthesized graphene using different techniques [36].

In this regard, a monolayer graphene film with metallic electrodes is transferred to a high impedance surface (HIS) which is realized by the printed circuit board (PCB) technology at microwave frequencies. The measurement is conducted in a small microwave chamber [37]. In another research in the same spectrum, an infrared laser is used to etch the CVD grown graphene sheet with predefined periodicity and later investigate the absorption of the designed structure inside a rectangular waveguide [38]. The electron beam lithography is another approach used for patterning the graphene sheet for enhanced light matter interaction [39]. Moreover, a transparent graphene millimeter wave absorber constructed by multiple transfer-etch processing is characterized by reflectometry technique at 140 GHz [40]. Also, CVD-grown graphene is used to enhance the sensitivity of the surface-enhanced Raman spectroscopy (SERS)-based chemical sensor. The measurement is done using a Raman spectrometer at the laser wavelength of 785 nm (red) [41]. In another sensor chip, DNA is hybridized to the graphene-based substrate under UV light with the wavelength of 260 nm. In this sensor, the atomic force microscopy (AFM) is used to ensure the continuity and uniformity of the synthesized graphene, and Raman characterization is used to investigate its quality and the number of layers [42].

2.1 Graphene material under electric bias

When a graphene sheet is under electric bias, its surface conductivity is isotropic and can be approximately calculated by using Kubo's formulas as [43]:

$$\sigma_{\text{intra}} = \frac{2ie^2k_B T}{\hbar^2\pi(\omega + i/\tau)} \ln \left[2 \cosh \left(\frac{\mu_c}{2k_B T} \right) \right] \quad (1)$$

$$\sigma_{\text{inter}} = \frac{e^2}{4\hbar} \times \left[\frac{1}{2} + \frac{1}{\pi} \arctan \left(\frac{\hbar\omega - 2\mu_c}{2k_B T} \right) - \frac{i}{2\pi} \ln \left(\frac{(\hbar\omega + 2\mu_c)^2}{(\hbar\omega - 2\mu_c)^2 + (2k_B T)^2} \right) \right] \quad (2)$$

In the above equations, T is the temperature, μ_c is the chemical potential of graphene, \hbar is the reduced Planck's constant, K_B is the Boltzmann's constant, and ω is the angular frequency. At low-THz frequencies, the inter-band contribution of the surface conductivity can be neglected. Also, the graphene layer can be modeled as a dielectric with very low thickness δ and equivalent dielectric constant $\epsilon = 1 - i\frac{\sigma}{\omega\epsilon_0\delta}$ [22]. Note that in the above equations, graphene is assumed to be in the linear region, otherwise, other terms proportional to $1/\omega^3$ and $1/\omega^4$ should be added respectively for the frequency range of $\hbar\omega < 2\mu_c$ and $\hbar\omega \geq 2\mu_c$ [44].

To increase the light-matter interaction of graphene material, the nano-patterning method has been proposed [45]. The surface conductivity of the periodic graphene

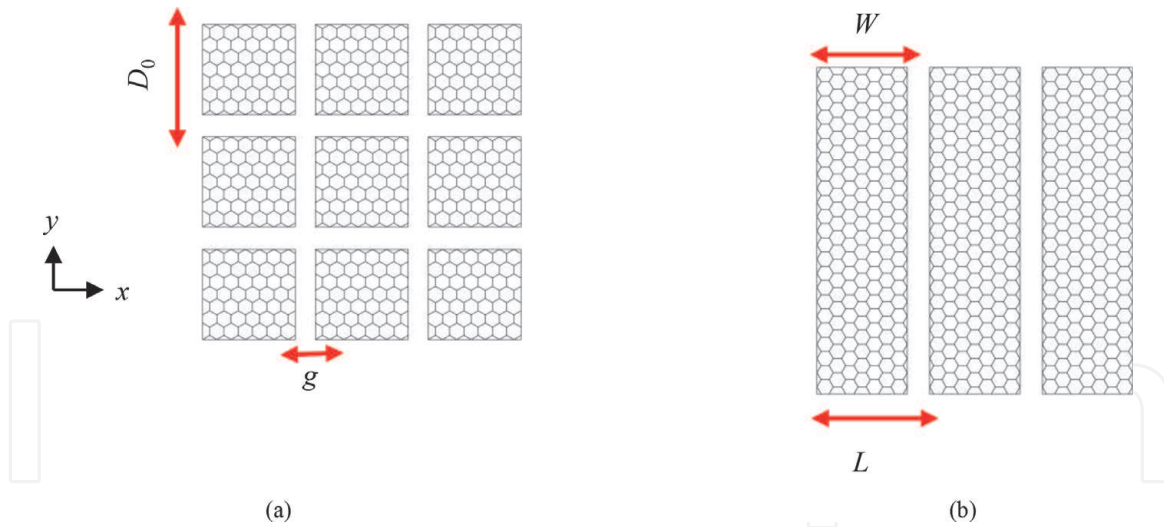


Figure 1. (a) Graphene square patches with the periodicity of D_0 and the air gap distance of g and (b) densely packed graphene strips with the width W and the periodicity L [46].

elements under the electric bias is also isotropic. For the square patches shown in **Figure 1(a)**, by considering the periodicity of D_0 and the air gap distance of g , closed-form surface impedance (inverse of the surface conductivity) is as [47]:

$$Z_s = \frac{D_0}{\sigma_s(D_0 - g)} + i \frac{\pi}{2\omega\epsilon_0 \left(\frac{\epsilon_2+1}{2}\right) D_0 \ln \left[\csc\left(\frac{\pi g}{2D_0}\right) \right]} \quad (3)$$

The effective surface conductivity of periodic graphene elements with arbitrary pattern can be measured or extracted using the parameter retrieval method through full-wave simulation [48]. It should be noted that for computing the electric field required for each considered chemical potential, approximate equations can be derived as [49]:

$$\mu_c(eV) = \begin{cases} \lambda_1 E_0^{\lambda_2}, E_0(V/nm) \geq 0 \\ -\lambda_1 E_0^{\lambda_2}, E_0(V/nm) < 0 \end{cases} \quad (4)$$

where, $\lambda_1 = 0.3677$ and $\lambda_2 = 0.5010$. For the chemical potentials in the range of $[-1,1]$ eV, the required bias fields are in the order of several volts per nanometer, which can be implemented practically [29].

The surface conductivity of densely packed graphene strips, as illustrated in **Figure 1(b)**, is anisotropic and can be approximated in the form of a diagonal tensor using the effective medium formulation as [50]:

$$\begin{aligned} \sigma_{xx} &= \frac{W\sigma\sigma_c}{L\sigma_c + W\sigma} \\ \sigma_{yy} &= \sigma \frac{W}{L} \\ \sigma_{xy} &= \sigma_{yx} = 0 \end{aligned} \quad (5)$$

In the above equations, W and L are the width and periodicity of the strips, respectively. Also, σ is the surface conductivity of graphene under electric bias, and σ_c is the static conductivity of the surface. Two very important properties of this environment are the existence of near-zero surface conductivity and hyperbolic dispersion region with the potential applications in 2D lens structures and the spontaneous emission enhancement of the dipole emitters [50, 51].

2.2 Graphene sheet with spatial dispersion effects

When the graphene sheet is placed on a substrate with a high dielectric constant, its surface conductivity is a tensor in which the elements depend on the wave propagation constant in the structure. This is called the spatial dispersion effect and the associated formulae for calculating surface conductivity are [29]:

$$\sigma_{xx} = \sigma + \alpha \frac{d^2}{dx^2} + \beta \frac{d^2}{dy^2} \quad (6)$$

$$\sigma_{yy} = \sigma + \beta \frac{d^2}{dx^2} + \alpha \frac{d^2}{dy^2} \quad (7)$$

$$\sigma_{xy} = \sigma_{yx} = 2\beta \frac{d^2}{dxdy} \quad (8)$$

The parameters σ , α , and β are extracted for an unbiased sheet ($\mu_c = 0$) through perturbation theory [29]. The resulting equations are valid for the electrically biased sheet ($\mu_c \neq 0$), as well [52].

2.3 Graphene sheet under magnetic bias

When a graphene sheet is under magnetic bias, its surface conductivity is also a tensor. The diagonal elements of this tensor are equal and the off-diagonal elements are opposite in sign defined as [53].

$$\sigma_{xx}(\omega, B_0) = \sigma_0 \frac{1 - i\omega\tau}{(\omega_c\tau)^2 + (1 - i\omega\tau)^2} \quad (9)$$

$$\sigma_{yx}(\omega, B_0) = \sigma_0 \frac{\omega_c\tau}{(\omega_c\tau)^2 + (1 - i\omega\tau)^2} \quad (10)$$

where $\sigma_0 = \frac{2e^2\tau}{\pi\hbar^2} k_B T \ln \left(2 \cosh \frac{\mu_c}{2k_B T} \right)$ and $\omega_c = \frac{eB_0 v_F^2}{\mu_c}$. The approximate formulas for the calculation of the surface impedance of the square graphene elements under magnetic bias, shown in **Figure 1(a)**, are as follows [54]:

$$\bar{\bar{Z}}_p = F_G \bar{\bar{Z}}_g + \frac{i}{2\alpha} \sqrt{\frac{\mu_0}{\epsilon_0 \epsilon_{eff}}} \begin{bmatrix} 1 & 0 \\ 0 & 1 \end{bmatrix} \quad (11)$$

where $F_G = 0.6[D_0/(D_0 - g)]^3 + 0.4$ and $\alpha = -\frac{k_0 D_0 \sqrt{\epsilon_{eff}}}{\pi} \ln \left[\sin \left(\frac{\pi g}{2D_0} \right) \right]$. Similar to the electrically biased patterned elements with arbitrary shapes, the parameter retrieval method can be used under the applied magnetic bias [55]. Given the discussion of the above three sections, it is observed that assuming the surface conductivity of graphene as:

$$\bar{\bar{\sigma}} = \begin{bmatrix} \sigma_{xx} & \sigma_{xy} \\ \sigma_{yx} & \sigma_{yy} \end{bmatrix} \quad (12)$$

All items expressed above can be extracted as a special case.

3. Analysis of graphene-based structures using dyadic Green's function

Dyadic Green's functions for the planarly, cylindrically, and spherically layered structures with graphene interfaces will be derived in this section. To this end, the

boundary conditions of the continuity and discontinuity of tangential electric and magnetic fields are respectively satisfied regarding the considered surface conductivity model for the graphene.

3.1 Graphene-based planarly layered media

This section aims to obtain dyadic Green's functions for planar structures with graphene boundaries. This problem can be solved either in the rectangular or cylindrical coordinates. In the first sub-section, a graphene sheet with the tensor surface conductivity boundary condition (TSCBC) is considered and its dyadic Green's function is calculated in the rectangular coordinates. In this case, the anisotropy of the surface impedance causes the coupling of the transverse electric (TE) and transverse magnetic (TM) fields. As a result of coupling, the number of unknown coefficients in the expansion of the dyadic Green's function is increased concerning the electrically biased sheet. In the second part of this section, a graphene-dielectric stack with an arbitrary number of layers is investigated considering the electric bias for the graphene sheets. This problem is solved in the cylindrical coordinates to simplify the calculation of the resulted Sommerfeld integrals.

3.1.1 Graphene sheet with the tensor surface conductivity boundary condition

The purpose of this section is to obtain the dyadic Green's function of a graphene sheet with the tensor surface conductivity in the interface of half-spaces, as shown in **Figure 2(a)**. The constitutive parameters of the top and bottom regions are considered as (ϵ_1, μ_1) and (ϵ_2, μ_2) , respectively. Without losing the generality of the problem, the source is assumed to be in the first environment and the graphene boundary is considered in $z = 0$ interface. Dyadic Green's function of this structure will be calculated using the scattering superposition method. For this purpose, the Green's function in each region of the problem is written in the form of the Green's function in the absence and presence of structure. Thus [23]:

$$\overline{\overline{G}}_e^{(11)} = \overline{\overline{G}}_{e0}(\overline{\mathbf{R}}, \overline{\mathbf{R}}') + \overline{\overline{G}}_{es}^{(11)}(\overline{\mathbf{R}}, \overline{\mathbf{R}}') \quad z > 0 \quad (13)$$

$$\overline{\overline{G}}_e^{(21)} = \overline{\overline{G}}_{es}^{(21)}(\overline{\mathbf{R}}, \overline{\mathbf{R}}') \quad z < 0 \quad (14)$$

where $\overline{\overline{G}}_{es}^{(11)}$ and $\overline{\overline{G}}_{es}^{(21)}$ are respectively the scattering Green's function in regions 1 and 2 and they are expanded in terms of $\overline{\mathbf{M}}$ and $\overline{\mathbf{N}}$ vector wave functions.

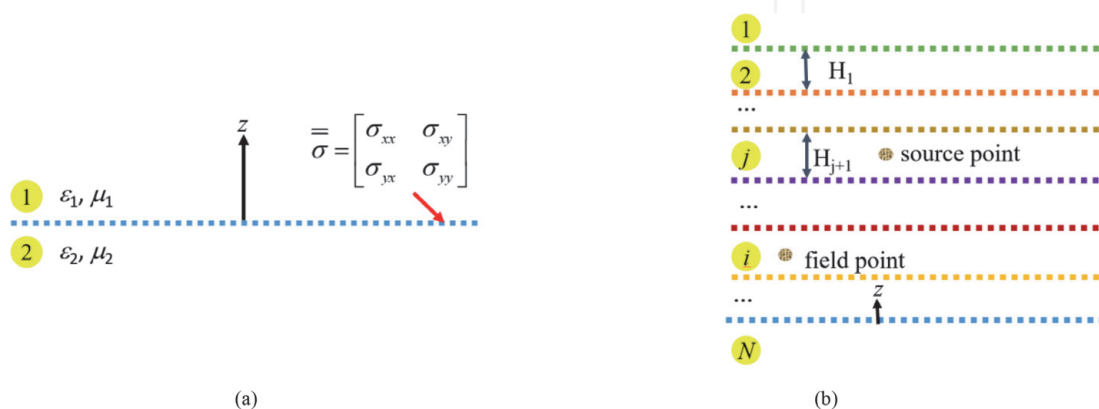


Figure 2.
 (a) Graphene sheet with the tensor surface conductivity boundary condition at the interface of half-spaces [46] and (b) graphene-dielectric stack.

Also, $\overline{\overline{\mathbf{G}}}_{e0}$ is the free-space Green's function which can be computed using the \mathbf{G}_m method as:

$$\begin{aligned} \overline{\overline{\mathbf{G}}}_{e0}(\overline{\mathbf{R}}, \overline{\mathbf{R}}') &= -\frac{1}{(k_1)^2} \hat{\mathbf{z}} \hat{\mathbf{z}} \delta(\overline{\mathbf{R}}, \overline{\mathbf{R}}') + \int_{-\infty}^{\infty} \int_{-\infty}^{\infty} dk_x dk_y C^{(1)} \\ &\times \left\{ \overline{\mathbf{M}}(-h_1) \overline{\mathbf{M}}'(h_1) + \overline{\mathbf{N}}(-h_1) \overline{\mathbf{N}}'(h_1) \right\} \quad z < z' \end{aligned} \quad (15)$$

where $C^{(1)} = \frac{i}{8\pi^2 h_1 (k_x^2 + k_y^2)}$. Using the scalar wave function $\psi(\overline{\mathbf{k}}) = \exp(ik_x x + ik_y y + ik_z z)$, it can be readily found that:

$$\overline{\mathbf{M}}(\overline{\mathbf{k}}) = i(k_y \hat{\mathbf{x}} - k_x \hat{\mathbf{y}}) \psi(\overline{\mathbf{k}}) \quad (16)$$

$$\overline{\mathbf{N}}(\overline{\mathbf{k}}) = \left(-\frac{k_z}{k_j} (k_x \hat{\mathbf{x}} + k_y \hat{\mathbf{y}}) + \frac{k_x^2 + k_y^2}{k_j} \hat{\mathbf{z}} \right) \psi(\overline{\mathbf{k}}) \quad (17)$$

The parameters k_x , k_y , and k_z are the wavenumbers in x , y , and z directions, respectively, and k_j shows the wavenumber for $j = 1, 2$. These parameters are not independent and are related to each other via $k_z = \pm \sqrt{k_j^2 - k_x^2 - k_y^2} = \pm \sqrt{k_j^2 - k_\rho^2}$. The vector wave function $\overline{\mathbf{M}}$ represents the electric field of TE modes and the vector wave function $\overline{\mathbf{N}}$ shows the electric field of the TM waves. In the structure under consideration, the anisotropy of surface conductivity leads to the coupling of TE and TM fields. Therefore [56]:

$$\begin{aligned} \overline{\overline{\mathbf{G}}}_{es}^{(11)}(\overline{\mathbf{R}}, \overline{\mathbf{R}}') &= \int_{-\infty}^{\infty} \int_{-\infty}^{\infty} dk_x dk_y C^{(1)} \times \left[(a_1 \overline{\mathbf{M}}(h_1) + a_1' \overline{\mathbf{N}}(h_1)) \overline{\mathbf{M}}'(h_1) \right. \\ &\left. + (b_1 \overline{\mathbf{N}}(h_1) + b_1' \overline{\mathbf{M}}(h_1)) \overline{\mathbf{N}}'(h_1) \right] \end{aligned} \quad (18)$$

$$\begin{aligned} \overline{\overline{\mathbf{G}}}_{es}^{(21)}(\overline{\mathbf{R}}, \overline{\mathbf{R}}') &= \int_{-\infty}^{\infty} \int_{-\infty}^{\infty} dk_x dk_y C^{(1)} \\ &\times \left[(a_2 \overline{\mathbf{M}}(-h_2) + a_2' \overline{\mathbf{N}}(-h_2)) \overline{\mathbf{M}}'(h_1) + (b_2 \overline{\mathbf{N}}(-h_2) + b_2' \overline{\mathbf{M}}(-h_2)) \overline{\mathbf{N}}'(h_1) \right] \end{aligned} \quad (19)$$

The unknown coefficients a_1 , a_1' , b_1 , b_1' , a_2 , a_2' , b_2 , and b_2' will be obtained by applying the boundary conditions. Using the self and mutual orthogonality of the vector wave functions, the above equations can be divided into two systems of equations, each with four unknown coefficients. The boundary conditions on the electric and magnetic Green's functions respectively state that:

$$\hat{\mathbf{z}} \times \left(\overline{\overline{\mathbf{G}}}_e^{(11)} - \overline{\overline{\mathbf{G}}}_e^{(21)} \right) = 0 \quad (20)$$

$$\hat{\mathbf{z}} \times \left(\frac{\nabla \times \overline{\overline{\mathbf{G}}}_e^{(11)}}{i\omega\mu_1} - \frac{\nabla \times \overline{\overline{\mathbf{G}}}_e^{(21)}}{i\omega\mu_2} \right) = \overline{\overline{\boldsymbol{\sigma}}}_e \cdot \overline{\overline{\mathbf{G}}}_e^{(21)} \quad (21)$$

After applying the above boundary conditions and removing the coupling effect from the tangential components of the electric field, and by defining, $A = \sigma_{xx} k_x + \sigma_{xy} k_y$, $B = \sigma_{yx} k_x + \sigma_{yy} k_y$, $C = \sigma_{xx} k_y - \sigma_{xy} k_x$, and, $D = \sigma_{yy} k_x - \sigma_{yx} k_y$,

the unknown coefficients of the TE waves, $a_1 = \frac{\Delta_{TE}^{(1)}}{\Delta_{TE}}$ and $a'_1 = \frac{\Delta_{TE}^{(2)}}{\Delta_{TE}}$, can be obtained as [46]:

$$\Delta_{TE} = ik_\rho^2 P^+ Q^+ + P^+ (Ak_x + Bk_y) i\omega \frac{h_1}{k_1} + Q^+ i\omega (Ck_y + Dk_x) + \omega^2 i \frac{h_1}{k_1} (BC + AD) \quad (22)$$

$$\Delta_{TE}^{(1)} = ik_\rho^2 Q^+ P^- + (Ak_x + Bk_y) P^- i\omega \frac{h_1}{k_1} - \omega i (Ck_y + Dk_x) Q^+ - \omega^2 i \frac{h_1}{k_1} (BC + AD) \quad (23)$$

$$\Delta_{TE}^{(2)} = \omega \frac{2h_1}{\mu_1} (Dk_y - Ck_x) \quad (24)$$

where, $P^+ = \frac{h_1}{\mu_1} + \frac{h_2}{\mu_2}$, $Q^+ = \frac{k_1}{\mu_1} + \frac{k_2^2 h_1}{k_1 h_2 \mu_2}$, $P^- = \frac{h_1}{\mu_1} - \frac{h_2}{\mu_2}$, and $Q^- = \frac{k_1}{\mu_1} - \frac{k_2^2 h_1}{k_1 h_2 \mu_2}$. By defining the TM waves expansion coefficients as $b_1 = \frac{\Delta_{TM}^{(1)}}{\Delta_{TM}}$ and $b'_1 = \frac{\Delta_{TM}^{(2)}}{\Delta_{TM}}$, it can be shown:

$$\Delta_{TM} = ik_\rho^2 Q^+ P^+ + i\omega Q^+ (Ck_y + Dk_x) + i\omega \frac{h_1}{k_1} P^+ (Ak_x + Bk_y) + i\omega^2 \frac{h_1}{k_1} (AD + BC) \quad (25)$$

$$\begin{aligned} \Delta_{TM}^{(1)} = & -ik_\rho^2 Q^- P^+ + i\omega \frac{h_1}{k_1} P^+ + (Ak_x + Bk_y) - i\omega (Dk_x + Ck_y) Q^- \\ & + i\omega^2 \frac{h_1}{k_1} (AD + BC) \end{aligned} \quad (26)$$

$$\Delta_{TM}^{(2)} = -2\omega \frac{h_1}{\mu_1} (Ak_y - Bk_x) \quad (27)$$

Other unknown coefficients can be obtained using decoupling equations in [46]. To validate the obtained coefficients, the structure of **Figure 1(a)** consisting of square patches with $D_0 = 5 \mu\text{m}$, $g = 0.5 \mu\text{m}$, $\mu_c = 0.5 \text{ eV}$ and $\tau = 0.5 \text{ ps}$ with plane wave illumination is considered under electric and magnetic biases. Since Green's function coefficients are the same as reflection and transmission coefficients of the plane wave, the results of Green's function are compared with the results of the circuit model as [54]:

$$S_{31} = \frac{2(2 + \eta_0 \sigma_d)}{(2 + \eta_0 \sigma_d)^2 + (\eta_0 \sigma_0)^2} \quad (28)$$

$$S_{41} = \frac{2\eta_0 \sigma_0}{(2 + \eta_0 \sigma_d)^2 + (\eta_0 \sigma_0)^2} \quad (29)$$

Figure 3 shows the magnitude of the transmission coefficient by considering the electric bias for the graphene layer. The results of the two methods are identical,

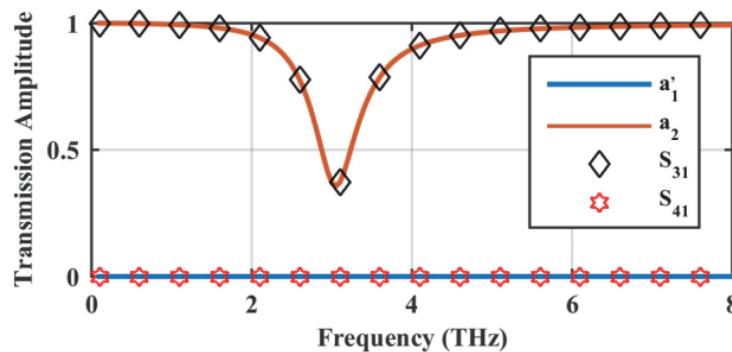
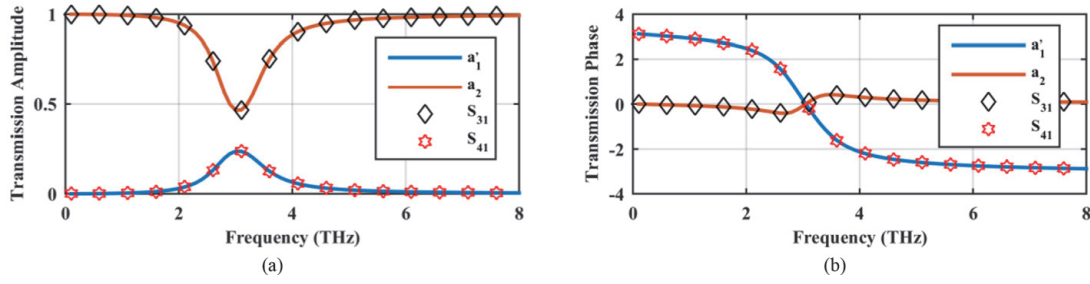


Figure 3. The magnitude of the transmission coefficient for the graphene nano-patch with the parameters $D_0 = 5 \mu\text{m}$, $g = 0.5 \mu\text{m}$, $\mu_c = 0.5 \text{ eV}$, and $\tau = 0.5 \text{ ps}$ [46].


Figure 4.

(a) The magnitude and (b) phase of the transmission coefficient for the graphene nano-patch with $D_o = 5 \mu\text{m}$, $g = 0.5 \mu\text{m}$, $\mu_c = 0.5 \text{ eV}$, $ps. \tau = 0.5$, and $B_o = 0.5 \text{ T}$ [46].

and because of the absence of electromagnetic coupling under electric bias, the transmission coefficient due to mutual coupling is zero. In **Figure 4** the same results are illustrated for the applied magnetic bias of 0.5 Tesla. There is good agreement in the magnitude and phase of the transmission coefficient in the abovementioned two methods. Also, by finding the poles of the coefficients, the electromagnetic wave propagation constants for the electrically and magnetically biased graphene sheets can be obtained which are in full agreement with [28, 57], respectively. The correctness of the extracted coefficients confirms the validity of the dyadic Green's function formulation.

3.1.2 Graphene-dielectric stack

Dyadic Green's function for an N -layer dielectric environment has been previously formulated using the scattering superposition method [58]. In this section, the above equations are extended to the environment with the electrically biased graphene boundaries, as shown in **Figure 2(b)**. The graphene boundary can be either continuous or periodically patterned as discussed in **section 2**. To start the analysis, the layers are numbered by starting from the top layer, and an arbitrary field point i and source point j are assumed. The problem is solved in the cylindrical coordinates. Since the cylindrical wave functions are discussed in detail in the next section, they are not mentioned here. The dyadic Green's function can be expanded as [58]:

$$\begin{aligned} \overline{\overline{\mathbf{G}}}_{es}^{(ij)}(\mathbf{r}, \mathbf{r}') = & \frac{i}{4\pi} \int_{-\infty}^{\infty} dh \sum_{n=0}^{\infty} \frac{(2 - \delta_n^0)}{\lambda h_j} \\ & \left\{ (1 - \delta_i^N) \overline{\mathbf{M}}_{n\lambda}(h_i) \left[(1 - \delta_j^1) A_M^{ij} \overline{\mathbf{M}}'_{n\lambda}(-h_j) + (1 - \delta_j^N) B_M^{ij} \overline{\mathbf{M}}'_{n\lambda}(h_j) \right] + \right. \\ & (1 - \delta_i^N) \overline{\mathbf{N}}_{n\lambda}(h_i) \left[(1 - \delta_j^1) A_N^{ij} \overline{\mathbf{N}}'_{n\lambda}(-h_j) + (1 - \delta_j^N) B_N^{ij} \overline{\mathbf{N}}'_{n\lambda}(h_j) \right] + \\ & (1 - \delta_i^1) \overline{\mathbf{M}}_{n\eta}(-h_i) \left[(1 - \delta_j^1) C_M^{ij} \overline{\mathbf{M}}'_{n\lambda}(-h_j) + (1 - \delta_j^N) D_M^{ij} \overline{\mathbf{M}}'_{n\lambda}(h_j) \right] + \\ & \left. (1 - \delta_i^1) \overline{\mathbf{N}}_{n\eta}(-h_i) \times \left[(1 - \delta_j^1) C_N^{ij} \overline{\mathbf{N}}'_{n\lambda}(-h_j) + (1 - \delta_j^N) D_N^{ij} \overline{\mathbf{N}}'_{n\lambda}(h_j) \right] \right\} \end{aligned} \quad (30)$$

In the above equations, $\overline{\mathbf{M}}$ and $\overline{\mathbf{N}}$ are vector wave functions in the cylindrical coordinate system, and $A_{M,N}^{ij}$, $B_{M,N}^{ij}$, $C_{M,N}^{ij}$, $D_{M,N}^{ij}$ are unknown coefficients. The Kronecker delta function is used in the field expansion to generalize the formulation for the arbitrary locations of the field and source points. By applying the boundary conditions on the tangential components of the electric field at the interface of the arbitrary two layers, denoted by i and $i + 1$, it can be shown that:

$$\begin{bmatrix} A_M^{ij} \\ B_M^{ij} \\ O_i A_N^{ij} \\ O_i B_N^{ij} \end{bmatrix} e^{ih_i z_i} + \begin{bmatrix} C_M^{ij} \\ D_M^{ij} + \delta_j^i \\ O_i C_N^{ij} \\ O_i (D_N^{ij} + \delta_j^i) \end{bmatrix} e^{-ih_i z_i} = \begin{bmatrix} (A_M^{(i+1)j} + \delta_{i+1}^j) \\ B_M^{(i+1)j} \\ O_{i+1} (A_N^{(i+1)j} + \delta_{i+1}^j) \\ O_{i+1} B_N^{(i+1)j} \end{bmatrix} e^{ih_{i+1} z_i} + \begin{bmatrix} C_M^{(i+1)j} \\ D_M^{(i+1)j} \\ O_{i+1} C_N^{(i+1)j} \\ O_{i+1} D_N^{(i+1)j} \end{bmatrix} e^{-ih_{i+1} z_i} \quad (31)$$

where $O_i = \frac{h_i}{k_i}$, $P_i = \frac{h_i}{\mu_i}$, $Q_i = \frac{k_i}{\mu_i}$. The boundary condition on the tangential components of the magnetic field yields:

$$\begin{bmatrix} P_{i+1} (A_M^{(i+1)j} + \delta_{i+1}^j) \\ P_{i+1} B_M^{(i+1)j} \\ Q_{i+1} (A_N^{(i+1)j} + \delta_{i+1}^j) \\ Q_{i+1} B_N^{(i+1)j} \end{bmatrix} e^{ih_{i+1} z_i} - \begin{bmatrix} P_{i+1} C_M^{(i+1)j} \\ P_{i+1} D_M^{(i+1)j} \\ Q_{i+1} C_N^{(i+1)j} \\ Q_{i+1} D_N^{(i+1)j} \end{bmatrix} e^{-ih_{i+1} z_i} - \begin{bmatrix} P_i A_M^{ij} \\ P_i B_M^{ij} \\ Q_i A_N^{ij} \\ Q_i B_N^{ij} \end{bmatrix} e^{ih_i z_i} + \begin{bmatrix} P_i C_M^{ij} \\ P_i (D_M^{ij} + \delta_j^i) \\ Q_i C_N^{ij} \\ Q_i (D_N^{ij} + \delta_j^i) \end{bmatrix} e^{-ih_i z_i} = i\omega\sigma_{(i+1)i} \begin{bmatrix} A_M^{ij} \\ B_M^{ij} \\ P_i A_N^{ij} \\ P_i B_N^{ij} \end{bmatrix} e^{ih_i z_i} + i\omega\sigma_{(i+1)i} \begin{bmatrix} C_M^{ij} \\ (D_M^{ij} + \delta_j^i) \\ P_i C_N^{ij} \\ P_i (D_N^{ij} + \delta_j^i) \end{bmatrix} e^{-ih_i z_i} \quad (32)$$

By re-writing the coefficients as a matrix:

$$\begin{bmatrix} A_{M,N}^{(i+1)j} + \delta_{i+1}^j & B_{M,N}^{(i+1)j} \\ C_{M,N}^{(i+1)j} & D_{M,N}^{(i+1)j} \end{bmatrix} = \begin{bmatrix} 1 & \frac{R_{Fi}^{H,V}}{T_{Fi}^{H,V}} \\ \frac{R_{Pi}^{H,V}}{T_{Pi}^{H,V}} & 1 \end{bmatrix} \begin{bmatrix} A_{M,N}^{ij} & B_{M,N}^{ij} \\ C_{M,N}^{ij} & D_{M,N}^{ij} + \delta_i^j \end{bmatrix} \quad (33)$$

the outgoing and incoming reflection and transmission coefficients can be defined and used to extract the recursive relations. The coefficients for \overline{M}' sources are:

$$R_{Fi}^H = \frac{\mu_i h_{i+1} - \mu_{i+1} h_i + g}{\mu_i h_{i+1} + \mu_{i+1} h_i + g} \quad (34)$$

$$R_{Pi}^H = \frac{\mu_i h_{i+1} - \mu_{i+1} h_i - g}{\mu_i h_{i+1} + \mu_{i+1} h_i - g} \quad (35)$$

$$T_{Fi}^H = \frac{2\mu_i h_{i+1}}{\mu_i h_{i+1} + \mu_{i+1} h_i + g} \quad (36)$$

$$T_{Pi}^H = \frac{2\mu_i h_{i+1}}{\mu_i h_{i+1} + \mu_{i+1} h_i - g} \quad (37)$$

The coefficients for \overline{N} sources are:

$$R_{Fi}^V = \frac{\mu_i h_i k_{i+1}^2 - k_i^2 \mu_{i+1} h_{i+1} + g h_i h_{i+1}}{\mu_i h_i k_{i+1}^2 + \mu_{i+1} h_{i+1} k_i^2 + g h_i h_{i+1}} \quad (38)$$

$$R_{Pi}^V = \frac{\mu_i h_i k_{i+1}^2 - \mu_{i+1} k_i^2 h_{i+1} - g h_i h_{i+1}}{\mu_i h_i k_{i+1}^2 + \mu_{i+1} k_i^2 h_{i+1} - g h_i h_{i+1}} \quad (39)$$

$$T_{Pi}^V = \frac{2\mu_{i+1} k_i k_{i+1} h_{i+1}}{\mu_i h_i k_{i+1}^2 + \mu_{i+1} k_i^2 h_{i+1} - g h_i h_{i+1}} \quad (40)$$

$$T_{Fi}^V = \frac{2\mu_i h_{i+1} k_i k_{i+1}}{\mu_i h_i k_{i+1}^2 + \mu_{i+1} h_{i+1} k_i^2 + g h_i h_{i+1}} \quad (41)$$

The superscripts H and V respectively denote TE and TM sources. Also, subscripts F and P are used to show the incoming and outgoing waves, respectively. The procedure of extracting the unknown coefficients using (34)-(41) is discussed in [58]. To validate the proposed formulas, a parallel plate waveguide with graphene walls is considered. To extract the characteristic equation using the proposed formulations, it is necessary to force the denominator of the coefficients equal to zero. For this three-layer medium:

$$T^{(1)} = T^2 \cdot T^1 = \begin{bmatrix} \frac{1}{T_{F2}^H} e^{i(h_2-h_1)d} & \frac{R_{F2}^H}{T_{F2}^H} e^{-i(h_2-h_1)d} \\ \frac{R_{P2}^H}{T_{P2}^H} e^{i(h_2+h_1)d} & \frac{1}{T_{P2}^H} e^{-i(h_2-h_1)d} \end{bmatrix} \cdot \begin{bmatrix} \frac{1}{T_{F1}^H} & \frac{R_{F1}^H}{T_{F1}^H} \\ \frac{R_{P1}^H}{T_{P1}^H} & \frac{1}{T_{P1}^H} \end{bmatrix} \quad (42)$$

From which it can be deduced that $B_{M,N}^{11} = -\frac{T_{12}^{(1)}}{T_{11}^{(1)}}$. By setting $T_{11}^{(1)}$ equal to zero and assuming that the medium (1) and (3) are the same, and also defining $h = i\omega\mu_1\sigma$, for the H coefficients it can be concluded that:

$$\frac{e^{ih_2d} - 1}{e^{ih_2d} + 1} h_1 - (h_2 + h) = 0 \Rightarrow h_2 + h + j \tan\left(\frac{h_2d}{2}\right) h_1 = 0 \quad (43)$$

This procedure is repeatable for V sources. Also, to calculate the reflection coefficient from a multilayer structure, it is necessary to consider the field and source points in region 1. In this case, the only non-zero coefficient in Green's function expansion is $B_{M,N}^{11}$ coefficient representing the plane wave reflection coefficient from the multilayer structure.

3.2 Graphene-based cylindrical structures

In this section, the dyadic Green's function of a cylindrical structure with the tensor surface conductivity boundary condition will be extracted. Later, different examples of guiding and scattering problems are provided to investigate the validity

of the formulation. In general, in cylindrical structures, TE and TM modes are coupled, which leads to the complexity of mathematical relations. Therefore, the generalization of the formulation to the multilayered cylinders is not considered here. Note that graphene sheets can be wrapped around cylindrical particles due to the presence of van der Waals force [59]. For this purpose, tape-assist transfer under micromanipulation and spin-coating methods are proposed [60].

3.2.1 Dyadic Green's function for a cylinder with tensor surface conductivity boundary condition

The dyadic Green's function of the single-layer cylinder with the tensor surface conductivity boundary condition, as considered in **Figure 5.**, will be extracted in the following. The interior region of the cylinder is made of dielectric material and its cover is considered as a full tensor surface conductivity. To solve the problem, the vector wave functions are defined as [23]:

$$\overline{\mathbf{M}}_\mu(h) = e^{im\phi} e^{ihz} \left[im \frac{Z_m(\mu r)}{r} \hat{r} - \frac{\partial Z_m(\mu r)}{\partial r} \hat{\phi} \right] \quad (44)$$

$$\overline{\mathbf{N}}_\mu(h) = \frac{1}{k_j} e^{im\phi} e^{ihz} \left[ih \frac{\partial Z_m(\mu r)}{\partial r} \hat{r} - \frac{hm}{r} Z_m(\mu r) \hat{\phi} - \mu^2 Z_m(\mu r) \hat{z} \right] \quad (45)$$

In the above equations, Z_m is the cylindrical Bessel function in the inner layer and the cylindrical Hankel function in the outer layer, both with the orders of m . The wavenumber in the radial direction is μ and the wavenumber along the length is h . The free-space Green's function in the cylindrical coordinates is [23]:

$$\begin{aligned} \overline{\mathbf{G}}_{e0}(\overline{\mathbf{R}}, \overline{\mathbf{R}}') &= -\frac{1}{k^2} \hat{r} \hat{r} \delta(\overline{\mathbf{R}} - \overline{\mathbf{R}}') \\ &+ \frac{i}{8\pi} \int_{-\infty}^{\infty} dh \sum_{m=-\infty}^{\infty} \frac{1}{\eta^2} \times \left[\overline{\mathbf{M}}_\eta(h) \overline{\mathbf{M}}_\eta'^{(1)}(-h) + \overline{\mathbf{N}}_\eta(h) \overline{\mathbf{N}}_\eta'^{(1)}(-h) \right] \quad R < R' \end{aligned} \quad (46)$$

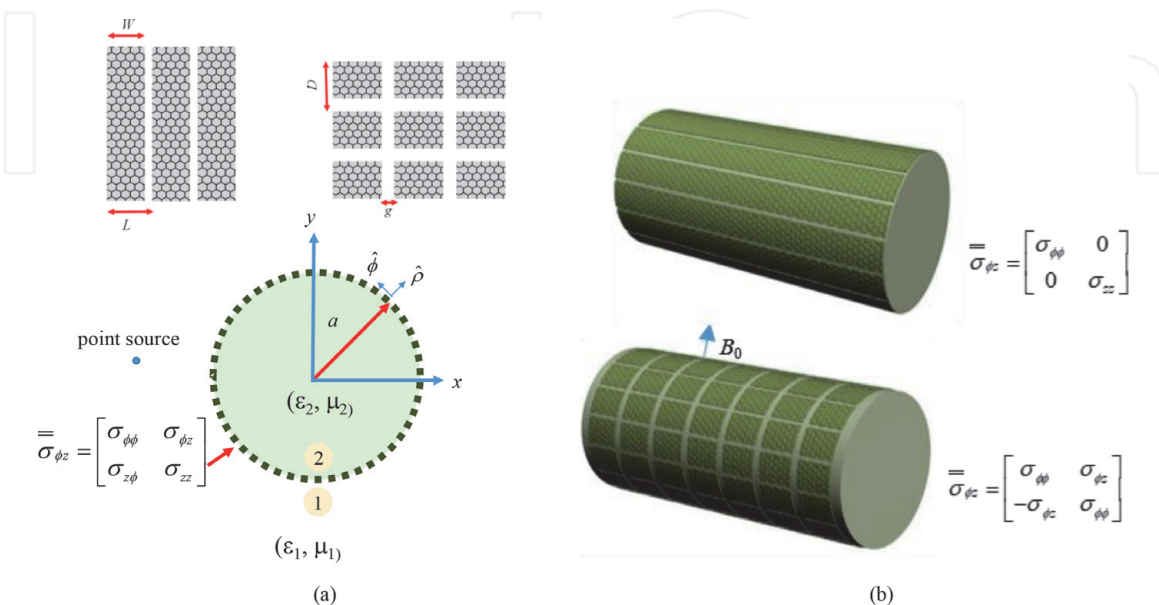


Figure 5. (a) A monolayer cylinder with a 2D cover with the tensor surface conductivity boundary condition and (b) its special cases constructed by densely packed strips and square nano-patches [61].

In the cylindrical coordinate system, TE and TM modes are coupled and the expansion of the fields are [23].

$$\overline{\overline{\mathbf{G}}}_{es}^{(11)}(\overline{\mathbf{R}}, \overline{\mathbf{R}}') = \frac{i}{8\pi} \int_{-\infty}^{\infty} dh \sum_{m=-\infty}^{\infty} \frac{1}{\eta^2} \times \left\{ \left[A_\eta \overline{\mathbf{M}}_\eta^{(1)}(h) + B_\eta \overline{\mathbf{N}}_\eta^{(1)}(h) \right] \overline{\mathbf{M}}_\eta'^{(1)}(-h) + \left[C_\eta \overline{\mathbf{N}}_\eta^{(1)}(h) + D_\eta \overline{\mathbf{M}}_\eta^{(1)}(h) \right] \overline{\mathbf{N}}_\eta'^{(1)}(-h) \right\} \quad (47)$$

$$\overline{\overline{\mathbf{G}}}_{es}^{(21)}(\overline{\mathbf{R}}, \overline{\mathbf{R}}') = \frac{i}{8\pi} \int_{-\infty}^{\infty} dh \sum_{m=-\infty}^{\infty} \frac{1}{\eta^2} \times \left\{ \left[a_\xi \overline{\mathbf{M}}_\xi(h) + b_\xi \overline{\mathbf{N}}_\xi(h) \right] \overline{\mathbf{M}}_\eta'^{(1)}(-h) + \left[c_\xi \overline{\mathbf{N}}_\xi(h) + d_\xi \overline{\mathbf{M}}_\xi(h) \right] \overline{\mathbf{N}}_\eta'^{(1)}(-h) \right\} \quad (48)$$

where A_η , B_η , C_η , and D_η are the unknown coefficients of the DGF expansion in region 1. Also, a_ξ , b_ξ , c_ξ , and d_ξ are DGF expansion coefficients in the region 2. The boundary condition on the tangential components of the magnetic Green's function is given by [61]:

$$\hat{\mathbf{r}} \times \left(\frac{\nabla \times \overline{\overline{\mathbf{G}}}_e^{(11)}}{\mu_1} - \frac{\nabla \times \overline{\overline{\mathbf{G}}}_e^{(21)}}{\mu_2} \right) = i\omega \overline{\overline{\boldsymbol{\sigma}}}_{\phi z} \cdot \overline{\overline{\mathbf{G}}}_e^{(21)} \quad (49)$$

By applying the above-mentioned boundary condition along with the boundary condition regarding the continuity of the electric Green's function to (47)–(48), the system of equations to determine the unknown coefficients can be obtained as:

$$\begin{bmatrix} -\frac{\partial H_m^{(1)}(\eta a)}{\partial a} & -\frac{1}{k_1} \frac{hm}{a} H_m^{(1)}(\eta a) & \frac{\partial J_m(\xi a)}{\partial a} & \frac{1}{k_2} \frac{hm}{a} J_m(\xi a) \\ 0 & -\frac{1}{k_1} \eta^2 H_m^{(1)}(\eta a) & 0 & \frac{1}{k_2} \xi^2 J_m(\xi a) \\ -\frac{1}{\mu_1} \frac{hm}{a} H_m^{(1)}(\eta a) & -\frac{k_1}{\mu_1} \frac{\partial H_m^{(1)}(\eta a)}{\partial a} & \frac{1}{\mu_2} \frac{hm}{a} J_m(\xi a) + \sigma_1 & \frac{k_2}{\mu_2} \frac{\partial J_m(\xi a)}{\partial a} + \sigma_2 \\ \frac{1}{\mu_1} \eta^2 H_m^{(1)}(\eta a) & 0 & -\frac{1}{\mu_2} \xi^2 J_m(\xi a) + \sigma_3 & \sigma_4 \end{bmatrix} \times \begin{bmatrix} A_\eta \\ B_\eta \\ a_\xi \\ b_\xi \end{bmatrix} = \begin{bmatrix} \frac{\partial J_m(\eta a)}{\partial a} \\ 0 \\ \frac{1}{\mu_1} \frac{hm}{a} J_m(\eta a) \\ -\frac{1}{\mu_1} \eta^2 J_m(\eta a) \end{bmatrix} \quad (50)$$

$$\begin{aligned}
 & \begin{bmatrix} -\frac{1}{k_1} \frac{hm}{a} H_m^{(1)}(\eta a) & -\frac{\partial H_m^{(1)}(\eta a)}{\partial a} & \frac{1}{k_2} \frac{hm}{a} J_m(\xi a) & \frac{\partial J_m(\xi a)}{\partial a} \\ -\frac{1}{k_1} \eta^2 H_m^{(1)}(\eta a) & 0 & \frac{1}{k_2} \xi^2 J_m(\xi a) & 0 \\ -\frac{k_1}{\mu_1} \frac{\partial H_m^{(1)}(\eta a)}{\partial a} & -\frac{1}{\mu_1} \frac{hm}{a} H_m^{(1)}(\eta a) & \frac{k_2}{\mu_2} \frac{\partial J_m(\xi a)}{\partial a} + \sigma'_1 & \frac{1}{\mu_2} \frac{hm}{a} J_m(\xi a) + \sigma'_2 \\ 0 & \frac{1}{\mu_1} \eta^2 H_m^{(1)}(\eta a) & \sigma'_3 & -\frac{1}{\mu_2} \xi^2 J_m(\xi a) + \sigma'_4 \end{bmatrix} \times \begin{bmatrix} C_\eta \\ D_\eta \\ c_\xi \\ d_\xi \end{bmatrix} \\
 & = \begin{bmatrix} \frac{1}{k_1} \frac{hm}{a} J_m(\eta a) \\ \frac{1}{k_1} \eta^2 J_m(\eta a) \\ \frac{k_1}{\mu_1} \frac{\partial J_m(\eta a)}{\partial a} \\ 0 \end{bmatrix}.
 \end{aligned} \tag{51}$$

where:

$$\begin{aligned}
 \sigma_1 &= i\omega\sigma_{z\phi} \frac{\partial J_m(\xi a)}{\partial a}, \sigma_2 = i\omega \frac{\sigma_{zz}}{k_2} \xi^2 J_m(\xi a) + i\omega\sigma_{z\phi} \frac{hm}{k_2 a} J_m(\xi a) \\
 \sigma_3 &= i\omega\sigma_{\phi\phi} \frac{\partial J_m(\xi a)}{\partial a}, \sigma_4 = i\omega\sigma_{\phi\phi} \frac{1}{k_2} \frac{hm}{a} J_m(\xi a) + i\omega\sigma_{\phi z} \frac{1}{k_2} \xi^2 J_m(\xi a) \\
 \sigma'_1 &= i\omega\sigma_{zz} \frac{1}{k_2} \xi^2 J_m(\xi a) + i\omega\sigma_{z\phi} \frac{hm}{k_2 a} J_m(\xi a), \sigma'_2 = i\omega\sigma_{z\phi} \frac{\partial J_m(\xi a)}{\partial a} \\
 \sigma'_3 &= i\omega\sigma_{\phi\phi} \frac{1}{k_2} \frac{hm}{a} J_m(\xi a) + i\omega\sigma_{\phi z} \frac{1}{k_2} \xi^2 J_m(\xi a), \sigma'_4 = i\omega\sigma_{\phi\phi} \frac{\partial J_m(\xi a)}{\partial a}
 \end{aligned}$$

Nullifying the determinant of the matrices (50)–(51) for $m = 0$, each of the above matrices can be separated as the multiplication of:

$$\frac{\omega\varepsilon_2 J_1(\xi a)}{\xi J_0(\xi a)} - \frac{\omega\varepsilon_1 H_1^{(1)}(\eta a)}{\eta H_0^{(1)}(\eta a)} + i\sigma_d = 0 \tag{52}$$

$$\frac{\xi J_0(\xi a)}{\omega\mu_2 J_1(\xi a)} - \frac{\eta H_0^{(1)}(\eta a)}{\omega\mu_1 H_1^{(1)}(\eta a)} + i\sigma_d = 0 \tag{53}$$

For the graphene shell under magnetic bias, both matrices in (50)–(51) result in the following equation for the propagation constant of hybrid TE and TM waves:

$$\left[\frac{\omega\varepsilon_2 H_1^{(1)}(-\xi a)}{\xi H_0^{(1)}(-\xi a)} - \frac{\omega\varepsilon_1 J_1(-\eta a)}{\eta J_0(-\eta a)} + i\sigma_d \right] \times \left[\frac{\eta J_0(-\eta a)}{\omega\mu_1 J_1(-\eta a)} - \frac{\xi H_0^{(1)}(-\xi a)}{\omega\mu_2 H_1^{(1)}(-\xi a)} + i\sigma_d \right] = -\sigma_0^2 \tag{54}$$

Which is in agreement with [57]. Also, the total scattering cross-section (TSCS) of a graphene-coated cylinder with the parameters $a = 50 \mu\text{m}$, $\varepsilon_2 = 2.4$, $\tau = 1 \text{ ps}$, $\mu_c = 0.25 \text{ eV}$ under electric bias is calculated for both TE and TM polarizations in

Figure 6, and compared with the results of the CST2017 software package. As can be seen, both methods have resulted in the same results.

As another example, the densely packed graphene strips with the parameters $L = 420$ nm, $W = 400$ nm, $\mu_c = 0.5$ eV, and $\tau = 1$ ps are considered around the dielectric cylinder as in **Figure 5**. It is assumed that the strips are wrapped around a hollow cylinder with the radius of $a = 50$ μm . **Figure 7** shows the TSCS of this structure for the magnetic biases with the strength in the range of 20-40 T. As observed, by increasing the magnetic bias, the resonant frequency of the surface plasmons blue shifts. The associated planar structure behaves as a hyperbolic meta-surface [62]. Under locally flat consideration of the curvature, this structure can also be considered as a hyperbolic medium. In the cylindrical geometries, hyperbolic meta-surfaces can be obtained using graphene-dielectric stacks [63]. The advantage of this hyperbolic structure is its two-dimensional nature and reconfigurability. It is also demonstrated that covering the surface of nanotubes with the hyperbolic meta-surface increases the interaction of the light with dipole emitters [64].

Finally, as **Figure 5(b)** illustrates, graphene-based square patches around the cylinder are considered under magnetic bias. Geometrical and optical parameters are as follows: $\tau = 1$ ps, $g = 0.5$ μm , and $D = 0.5$ μm and the TSCS is illustrated in **Figure 8**. for $B_0 = 0$ T and $B_0 = 10$ T. As can be seen, by changing the magnetic bias, the optical state changes from the maximum scattering to the minimum scattering. Such capability has recently been proposed by using a phase change material for switching between these two situations [65]. In this structure, the operating frequency can also be adjusted by changing the electric bias of graphene.

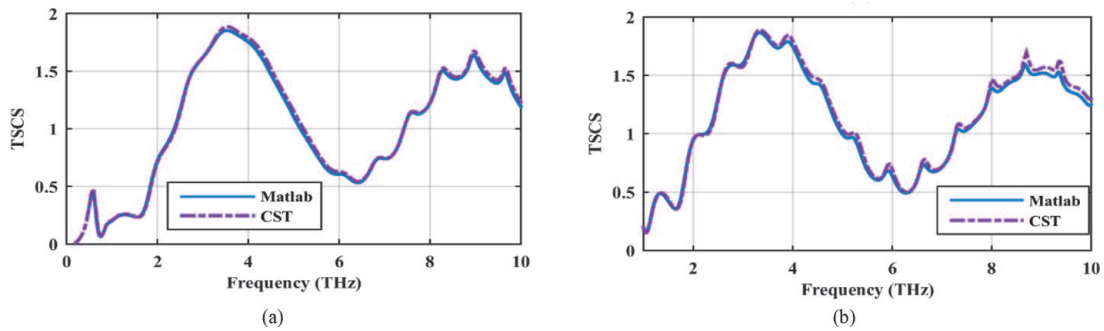


Figure 6. TSCS for an infinite cylinder covered with electrically biased graphene shell with $a = 50$ μm , $\epsilon_2 = 2.4$, $\tau = 1$ ps, and $\mu_c = 0.25$ eV considering (a) TE and (b) TM polarization for the incident wave [61].

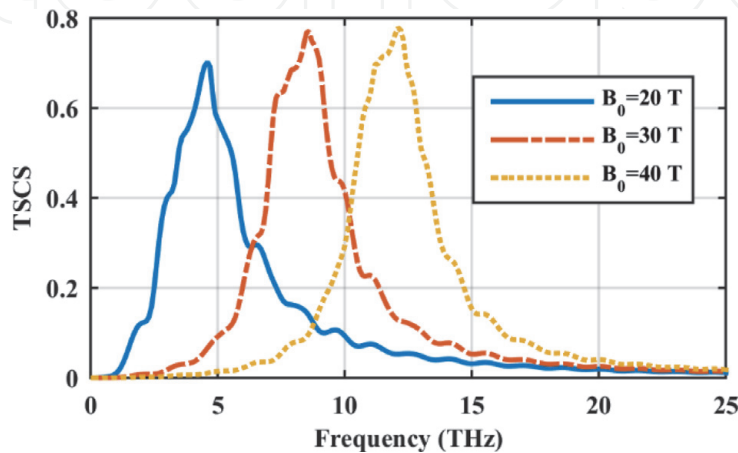


Figure 7. TSCS for an infinite length hollow cylinder ($a = 50$ μm) coated with densely packed graphene strips with $L = 420$ nm, $W = 400$ nm, $\mu_c = 0.5$ eV, and $\tau = 1$ ps considering different magnetic biases [61].

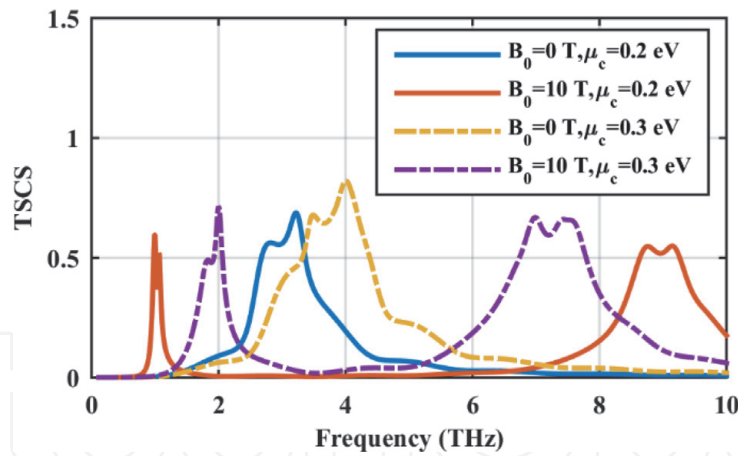


Figure 8. TSCS for an infinite cylinder coated with graphene patches with $D = 0.5 \mu\text{m}$, $g = 0.5 \mu\text{m}$, and $\tau = 0.5 \text{ps}$ under different electric and magnetic biases [61].

It is essential to note that in the cylindrical structures, the spatial domain Green's function consists of an integral on the real axis. Due to the existence of poles in the integration path, the integration path is usually deformed into a triangular shape. Also, a common method for calculating the spatial domain Green's function is the generalized pencil of function (GPOF) method in which the Green's function is expanded in terms of the complex exponential functions [66]. The unknowns can be found via the algorithm provided in [67]. Also, as mentioned earlier, the dyadic Green's function of the graphene-based multilayered cylindrical structures will not be considered here. For calculating the scattering cross-section of graphene-based multilayer cylindrical structures, a simple approach based on the transfer matrix method (TMM) is proposed that will be suitable for establishing novel optical devices [68, 69].

3.3 Graphene-based spherically layered medium

In this section, a multi-layered spherical structure with the graphene boundaries is considered and its Green's function is extracted by assuming different locations for the source and observation points. The relationship between the Green's function expansion coefficients and the modified Mie-Lorentz coefficients is exhibited to discuss how to solve the scattering problems using the Green's function. Scattering analysis of graphene-based layered structures is of great importance in the design of novel optical devices [70]. Finally, the procedure for calculating the Purcell factor is considered as an important application. Instances of experimentally realized graphene-coated spherical particles can be found in [71, 72], where improved template method and hydrothermal method are proposed for the synthesis. Also, transmission electron microscopy (TEM) and field emission scanning electron microscopy (FE-SEM) are used for characterization.

3.3.1 Dyadic Green's function of a graphene-based spherically layered structure

Let us consider an N -layer spherical medium with the graphene boundaries as shown in **Figure 9**. The purpose of this section is to compute the dyadic Green's function of this structure with the assumption of arbitrary locations for the field and source points. For this purpose, the Green's function in each layer is expanded in terms of vector wave functions with unknown coefficients. These functions are calculated using the scalar wave function of [74]:

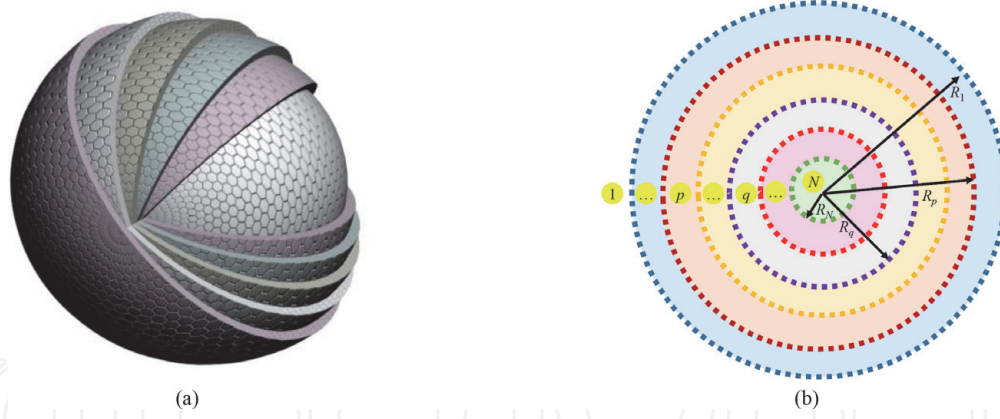


Figure 9. Spherically layered medium with graphene boundaries (a) 2D and (b) 3D views [73].

$$\varphi_{mn}(r, \theta, \phi) = z_n(k_p r) P_n^m(\cos \theta) e^{im\phi} \quad (55)$$

where $z_n(\cdot)$ represents the spherical Bessel or Hankel functions of order n and $P_n^m(\cdot)$ is the associated Legendre function with degree n and order m . It can be readily shown that:

$$\overline{\mathbf{M}}_{mn}(k_p) = z_n(k_p r) e^{im\phi} \left[\frac{im}{\sin \theta} P_n^m(\cos \theta) \hat{\boldsymbol{\theta}} - \frac{dP_n^m(\cos \theta)}{d\theta} \hat{\boldsymbol{\phi}} \right] \quad (56)$$

$$\begin{aligned} \overline{\mathbf{N}}_{mn}(k_p) &= \frac{n(n+1)}{k_p r} z_n(k_p r) P_n^m(\cos \theta) e^{im\phi} \hat{\mathbf{r}} + \\ &\frac{1}{k_p r} \frac{d[rz_n(k_p r)]}{dr} \left[\frac{dP_n^m(\cos \theta)}{d\theta} \hat{\boldsymbol{\theta}} + \frac{im}{\sin \theta} P_n^m(\cos \theta) \hat{\boldsymbol{\phi}} \right] e^{im\phi} \end{aligned} \quad (57)$$

The above vector functions are self and mutually orthogonal. This feature will be used to decouple the equation when computing the unknown coefficients.

As mentioned earlier, in the scattering superposition method, the dyadic Green's function is written as the sum of the free-space and scattering Green's functions. The free-space Green's function is related to the source in an infinite homogeneous medium while the scattering Green's function is due to the source in the presence of the layered medium. The expansion of the Green's function for the spherical structure with N concentric layers, assuming that the source and field points are respectively located in the desired layers with the labels p and q , can be written as [23]:

$$\overline{\overline{\mathbf{G}}}_e^{(pq)}(\mathbf{r}, \mathbf{r}') = \overline{\overline{\mathbf{G}}}_{0e}^{(pq)}(\mathbf{r}, \mathbf{r}') \delta_q^p + \overline{\overline{\mathbf{G}}}_{es}^{(pq)}(\mathbf{r}, \mathbf{r}') \quad (58)$$

The free-space Green's function can be obtained using the residue theorem as [23]:

$$\begin{aligned} \overline{\overline{\mathbf{G}}}_{0e}(\mathbf{r}, \mathbf{r}') &= -\frac{\hat{\mathbf{r}}\hat{\mathbf{r}}}{k_q^2} \delta(\mathbf{r} - \mathbf{r}') + \frac{ik_q}{4\pi} \sum_{n=1}^{\infty} \sum_{m=-n}^n (2 - \delta_m^0) \frac{2n+1}{n(n+1)} \times \\ &\frac{(n-m)!}{(n+m)!} \times \begin{cases} \overline{\mathbf{M}}_{mn}^{(1)}(k_q) \overline{\mathbf{M}}'_{mn}(k_q) + \overline{\mathbf{N}}_{mn}^{(1)}(k_q) \overline{\mathbf{N}}'_{mn}(k_q) & r > r' \\ \overline{\mathbf{M}}_{mn}(k_q) \overline{\mathbf{M}}'^{(1)}_{mn}(k_q) + \overline{\mathbf{N}}_{mn}(k_q) \overline{\mathbf{N}}'^{(1)}_{mn}(k_q) & r < r' \end{cases} \end{aligned} \quad (59)$$

Moreover, scattering Green's function in each layer can be expanded as [75]:

$$\begin{aligned} \overline{\overline{\mathbf{G}}}_{es}^{(pq)}(\mathbf{r}, \mathbf{r}') = & \frac{ik_q}{4\pi} \sum_{n=1}^{\infty} \sum_{m=-n}^n (2 - \delta_m^0) \frac{2n+1}{n(n+1)} \frac{(n-m)!}{(n+m)!} \times \\ & \left\{ (1 - \delta_p^N) \overline{\overline{\mathbf{M}}}_{mn}^{(1)} \left[(1 - \delta_q^1) A_H^{pq} \overline{\overline{\mathbf{M}}}'_{mn} + (1 - \delta_q^N) B_H^{pq} \overline{\overline{\mathbf{M}}}'_{mn} \right] \right. \\ & + (1 - \delta_p^N) \overline{\overline{\mathbf{N}}}_{mn}^{(1)} \left[(1 - \delta_q^1) A_V^{pq} \overline{\overline{\mathbf{N}}}'_{mn} + (1 - \delta_q^N) B_V^{pq} \overline{\overline{\mathbf{N}}}'_{mn} \right] \\ & + (1 - \delta_p^1) \overline{\overline{\mathbf{M}}}_{mn} \left[(1 - \delta_q^1) C_H^{pq} \overline{\overline{\mathbf{M}}}'_{mn} + (1 - \delta_q^N) D_H^{pq} \overline{\overline{\mathbf{M}}}'_{mn} \right] \\ & \left. + (1 - \delta_p^1) \overline{\overline{\mathbf{N}}}_{mn} \left[(1 - \delta_q^1) C_V^{pq} \overline{\overline{\mathbf{N}}}'_{mn} + (1 - \delta_q^N) D_V^{pq} \overline{\overline{\mathbf{N}}}'_{mn} \right] \right\} \end{aligned} \quad (60)$$

where $A_{H,V}^{pq}$, $B_{H,V}^{pq}$, $C_{H,V}^{pq}$, and $D_{H,V}^{pq}$ are the unknown coefficients of the Green's function to be obtained. In the above formulation, the superscript (1) represents that the spherical Hankel functions of the first type are chosen to represent the spherical vector functions. For the other vector wave functions, the first-kind Bessel function should be selected. As observed, in the spherical structures the TE and TM waves are not coupled. Thus, the expansion of the fields only includes the interaction of the functions $\overline{\overline{\mathbf{M}}}$ and $\overline{\overline{\mathbf{M}}}'$ as well as the functions $\overline{\overline{\mathbf{N}}}$ and $\overline{\overline{\mathbf{N}}}'$. Moreover, to solve the problem for the structures with the arbitrary number of layers, the Kronecker delta function is used in the expansions of the fields. In the middle layers of the spherical structure, the electric field is a linear combination of the Bessel and Hankel functions, whereas in the outermost layer, only the Hankel functions, and in the innermost layer, only the Bessel functions will exist. So we have used $(1 - \delta_p^1)$ and $(1 - \delta_p^N)$ functions. To determine the delta functions related to the source terms, free-space Green's function can be used. For $q = 1$ (external layer), the source functions related to the second criterion of the free-space Green's function is used. Also, for $q = N$ (internal layer) the source functions related to the first criterion should be used. In the middle layers, a linear combination of different source functions must be used.

It should be noted that by using the addition theorem in Legendre functions, the internal series in the Green's function expansion can be eliminated [11]. To select the number of terms required for the convergence of the external series, the conditions of the problem must be considered. In the other words, in the structures whose electrical size is very much smaller than that of the wavelength, the term $n = 1$ is sufficient for the convergence [76]. Also, in the case where the distance between the source and observation points is large, the series can be truncated in the number $N_t = x + 3\sqrt{x} + 2$, where $x = k_0 R_1$. Otherwise, the convergence of the series is weak, and a large number of terms in the range of $20 k_0 R_1$ should be considered. In this case, the series acceleration techniques will be highly efficient in terms of computational efficiency [77, 78].

Boundary conditions on tangential components of electric and magnetic Green's functions in the interface of two adjacent layers are [73]:

$$\hat{\mathbf{r}} \times \overline{\overline{\mathbf{G}}}_e^{(pq)} = \hat{\mathbf{r}} \times \overline{\overline{\mathbf{G}}}_e^{[(p+1)q]} \quad (61)$$

$$\frac{1}{i\omega\mu_{p+1}} \hat{\mathbf{r}} \times \nabla \times \overline{\overline{\mathbf{G}}}_e^{[(p+1)q]} - \frac{1}{i\omega\mu_p} \hat{\mathbf{r}} \times \nabla \times \overline{\overline{\mathbf{G}}}_e^{(pq)} = -\sigma_{(p+1)p} \hat{\mathbf{r}} \times \left(\hat{\mathbf{r}} \times \overline{\overline{\mathbf{G}}}_e^{(pq)} \right) \quad (62)$$

which respectively lead to the following equations:

$$\begin{bmatrix} \xi_n^{pp} A_H^{pq} \\ \xi_n^{pp} B_H^{pq} \\ \partial \xi_n^{pp} A_V^{pq} \\ \partial \xi_n^{pp} B_V^{pq} \end{bmatrix} + \begin{bmatrix} \psi_n^{pp} C_H^{pq} \\ \psi_n^{pp} (D_H^{pq} + \delta_p^q) \\ \partial \psi_n^{pp} C_V^{pq} \\ \partial \psi_n^{pp} (D_V^{pq} + \delta_p^q) \end{bmatrix} = \begin{bmatrix} \xi_n^{(p+1)p} (A_H^{(p+1)q} + \delta_{p+1}^q) \\ \xi_n^{(p+1)p} B_H^{(p+1)q} \\ \partial \xi_n^{(p+1)p} (A_V^{(p+1)q} + \delta_{p+1}^q) \\ \partial \xi_n^{(p+1)p} B_V^{(p+1)q} \end{bmatrix} + \begin{bmatrix} \psi_n^{(p+1)p} C_H^{(p+1)q} \\ \psi_n^{(p+1)p} D_H^{(p+1)q} \\ \partial \psi_n^{(p+1)p} C_V^{(p+1)q} \\ \partial \psi_n^{(p+1)p} D_V^{(p+1)q} \end{bmatrix} \quad (63)$$

$$\begin{aligned}
 & \frac{k_{p+1}}{\mu_{p+1}} \begin{bmatrix} \partial \xi_n^{(p+1)p} (A_H^{(p+1)q} + \delta_{p+1}^q) \\ \partial \xi_n^{(p+1)p} B_H^{(p+1)q} \\ \xi_n^{(p+1)p} (A_V^{(p+1)q} + \delta_{p+1}^q) \\ \xi_n^{(p+1)p} B_V^{(p+1)q} \end{bmatrix} + \frac{k_{p+1}}{\mu_{p+1}} \begin{bmatrix} \partial \psi_n^{(p+1)p} C_H^{(p+1)q} \\ \partial \psi_n^{(p+1)p} D_H^{(p+1)q} \\ \psi_n^{(p+1)p} C_V^{(p+1)q} \\ \psi_n^{(p+1)p} D_V^{(p+1)q} \end{bmatrix} - \frac{k_p}{\mu_p} \begin{bmatrix} \partial \xi_n^{pp} A_H^{pq} \\ \partial \xi_n^{pp} B_H^{pq} \\ \xi_n^{pp} A_V^{pq} \\ \xi_n^{pp} B_V^{pq} \end{bmatrix} - \\
 & \frac{k_p}{\mu_p} \begin{bmatrix} \partial \psi_n^{pp} C_H^{pq} \\ \partial \psi_n^{pp} (D_H^{pq} + \delta_p^q) \\ \psi_n^{pp} C_V^{pq} \\ \psi_n^{pp} (D_V^{pq} + \delta_p^q) \end{bmatrix} = \sigma^{(p+1)p} \begin{bmatrix} \xi_n^{pp} A_H^{pq} \\ \xi_n^{pp} B_H^{pq} \\ \partial \xi_n^{pp} A_V^{pq} \\ \partial \xi_n^{pp} B_V^{pq} \end{bmatrix} + \sigma^{(p+1)p} \begin{bmatrix} \psi_n^{pp} C_H^{pq} \\ \psi_n^{pp} (D_H^{pq} + \delta_p^q) \\ \partial \psi_n^{pp} C_V^{pq} \\ \partial \psi_n^{pp} (D_V^{pq} + \delta_p^q) \end{bmatrix} \quad (64)
 \end{aligned}$$

In the above equations, $\psi_n^{pq} = j_n(k_p R_q)$, $\xi_n^{pq} = h_n^{(1)}(k_p R_q)$, $\partial \psi_n^{pq} = 1/\rho d[\rho j_n(\rho)]|_{\rho=k_p R_q}$ and $\partial \xi_n^{pq} = 1/\rho d[\rho h_n^{(1)}(\rho)]|_{\rho=k_p R_q}$. To obtain recursive relations for unknown coefficients of Green's function, separating the above equations is necessary. Therefore [75]:

$$\begin{bmatrix} A_{H,V}^{(p+1)q} + \delta_{p+1}^q \\ B_{H,V}^{(p+1)q} \end{bmatrix} = \frac{1}{T_{Fp}^{H,V}} \begin{bmatrix} A_{H,V}^{pq} \\ B_{H,V}^{pq} \end{bmatrix} + \frac{R_{Fp}^{H,V}}{T_{Fp}^{H,V}} \begin{bmatrix} C_{H,V}^{pq} \\ D_{H,V}^{pq} + \delta_p^q \end{bmatrix} \quad (65)$$

$$\begin{bmatrix} C_{H,V}^{(p+1)q} \\ D_{H,V}^{(p+1)q} \end{bmatrix} = \frac{R_{Pp}^{H,V}}{T_{Pp}^{H,V}} \begin{bmatrix} A_{H,V}^{pq} \\ B_{H,V}^{pq} \end{bmatrix} + \frac{1}{T_{Pp}^{H,V}} \begin{bmatrix} C_{H,V}^{pq} \\ D_{H,V}^{pq} + \delta_p^q \end{bmatrix} \quad (66)$$

where the reflection and transmission coefficients for TE waves are computed as:

$$R_{Fp}^H = \frac{k_{p+1} \mu_p \partial \psi_n^{(p+1)p} \psi_n^{pp} - k_p \mu_{p+1} \partial \psi_n^{pp} \psi_n^{(p+1)p} + g \psi_n^{pp} \psi_n^{(p+1)p}}{k_{p+1} \mu_p \partial \psi_n^{(p+1)p} \xi_n^{pp} - k_p \mu_{p+1} \partial \xi_n^{pp} \psi_n^{(p+1)p} + g \xi_n^{pp} \psi_n^{(p+1)p}} \quad (67)$$

$$R_{Pp}^H = \frac{k_{p+1} \mu_p \partial \xi_n^{(p+1)p} \xi_n^{pp} - k_p \mu_{p+1} \partial \xi_n^{pp} \xi_n^{(p+1)p} + g \xi_n^{pp} \xi_n^{(p+1)p}}{k_{p+1} \mu_p \partial \xi_n^{(p+1)p} \psi_n^{pp} - k_p \mu_{p+1} \partial \psi_n^{pp} \xi_n^{(p+1)p} + g \psi_n^{pp} \xi_n^{(p+1)p}} \quad (68)$$

$$T_{Fp}^H = \frac{k_{p+1}\mu_p \left(\partial \psi_n^{(p+1)p} \xi_n^{(p+1)p} - \psi_n^{(p+1)p} \partial \xi_n^{(p+1)p} \right)}{k_{p+1}\mu_q \partial \psi_n^{(p+1)p} \xi_n^{pp} - k_p \mu_{p+1} \partial \xi_n^{pp} \psi_n^{(p+1)p} + g \xi_n^{pp} \psi_n^{(p+1)p}} \quad (69)$$

$$T_{Pp}^H = \frac{k_{p+1}\mu_p \left(\partial \xi_n^{(p+1)p} \psi_n^{(p+1)p} - \psi_n^{(p+1)p} \partial \xi_n^{(p+1)p} \right)}{k_{p+1}\mu_p \partial \xi_n^{(p+1)p} \psi_n^{pp} - k_p \mu_{p+1} \partial \psi_n^{pp} \xi_n^{(p+1)p} + g \psi_n^{pp} \xi_n^{(p+1)p}} \quad (70)$$

Also, the reflection and transmission coefficients for the TM waves are:

$$R_{Fp}^V = \frac{k_{p+1}\mu_p \psi_n^{(p+1)p} \partial \psi_n^{pp} - k_p \mu_{p+1} \psi_n^{pp} \partial \psi_n^{(p+1)p} + g \partial \psi_n^{pp} \partial \psi_n^{(p+1)p}}{k_{p+1}\mu_p \psi_n^{(p+1)p} \partial \xi_n^{pp} - k_p \mu_{p+1} \xi_n^{pp} \partial \psi_n^{(p+1)p} + g \partial \xi_n^{pp} \partial \psi_n^{(p+1)p}} \quad (71)$$

$$R_{Pp}^V = \frac{k_{p+1}\mu_p \psi_n^{(p+1)p} \partial \psi_n^{pp} - k_p \mu_{p+1} \psi_n^{pp} \partial \psi_n^{(p+1)p} + g \partial \psi_n^{pp} \partial \psi_n^{(p+1)p}}{k_{p+1}\mu_p \psi_n^{(p+1)p} \partial \xi_n^{pp} - k_p \mu_{p+1} \xi_n^{pp} \partial \psi_n^{(p+1)p} + g \partial \xi_n^{pp} \partial \psi_n^{(p+1)p}} \quad (72)$$

$$T_{Fp}^V = \frac{k_{p+1}\mu_p \left(\psi_n^{(p+1)p} \partial \xi_n^{(p+1)p} - \xi_n^{(p+1)p} \partial \psi_n^{(p+1)p} \right)}{k_{p+1}\mu_p \psi_n^{(p+1)p} \partial \xi_n^{pp} - k_p \mu_{p+1} \xi_n^{pp} \partial \psi_n^{(p+1)p} + g \partial \xi_n^{pp} \partial \psi_n^{(p+1)p}} \quad (73)$$

$$T_{Pp}^V = \frac{k_{p+1}\mu_p \left(\xi_n^{(p+1)p} \partial \psi_n^{(p+1)p} - \psi_n^{(p+1)p} \partial \xi_n^{(p+1)p} \right)}{k_{p+1}\mu_p \xi_n^{(p+1)p} \partial \psi_n^{pp} - k_p \mu_{p+1} \psi_n^{pp} \partial \xi_n^{(p+1)p} + g \partial \psi_n^{pp} \partial \xi_n^{(p+1)p}} \quad (74)$$

In the above formulas, the subscripts F and P represent the outgoing and incoming waves, respectively. The symbols $T_{(P,F)p}^H$ and $R_{(P,F)p}^H$ express the transmission and reflection of TE waves (due to the presence of superscript H), whereas the expression $T_{(P,F)p}^V$ and $R_{(P,F)p}^V$ express the transmission and reflection of the TM waves (due to the presence of superscript V). Using the matrix form:

$$\begin{bmatrix} A_{H,V}^{(p+1)q} + \delta_{p+1}^q & B_{H,V}^{(p+1)q} \\ C_{H,V}^{(p+1)q} & D_{H,V}^{(p+1)q} \end{bmatrix} = \begin{bmatrix} 1 & R_{Fp}^{H,V} \\ \frac{T_{Fp}^{H,V}}{T_{Fp}^{H,V}} & \frac{T_{Fp}^{H,V}}{T_{Fp}^{H,V}} \\ R_{Pp}^{H,V} & 1 \\ \frac{T_{Pp}^{H,V}}{T_{Pp}^{H,V}} & \frac{T_{Pp}^{H,V}}{T_{Pp}^{H,V}} \end{bmatrix} \begin{bmatrix} A_{H,V}^{pq} & B_{H,V}^{pq} \\ C_{H,V}^{pq} & D_{H,V}^{pq} + \delta_p^q \end{bmatrix} \quad (75)$$

Recursive relations can use to start through: $A_{H,V}^{Nq} = B_{H,V}^{Nq} = C_{H,V}^{1q} = D_{H,V}^{1q} = 0$.

It should be noted that due to the difficulty of constructing multiple concentric graphene shells, one can consider each boundary as a dielectric or perfect electric conductor (PEC) in the optical design. For example, an optical absorber consisting of a metal-dielectric spherical resonator whose outermost layer is coated with graphene is shown to enhance the absorption of the resonator [79]. To design optical structures such as absorber and invisible cloaks using Green's function formulation, it is necessary to transfer the point source to infinity to resemble a plane wave. In this case, considering the expansion of Green's function, it can be observed that the only unknown coefficients of expansion are $B_{H,V}^{pq}$ and $D_{H,V}^{pq}$ coefficients. Using the convolution integral it can be shown that [23]:

$$\overline{\overline{G}}_{0e} \cdot J + \overline{\overline{G}}_{es}^{(11)} \cdot J = \overline{\overline{G}}_{es}^{(21)} \cdot J \quad (76)$$

The source dependency is the same in all of the above Green's functions and can be simplified from both sides of the equation. It is observed that the equation is converted into the equation resulting from the Mie analysis of the spherically layered structures. By directly starting from the Mie-Lorentz theory, the same results can be obtained [80]. Moreover, due to the sub-wavelength nature of the localized graphene plasmons, the final formulas can be simplified using the polynomial approximation of the special functions [81]. These structures can also be used as the building blocks of optical meta-materials [82].

3.3.2 Purcell factor and energy transfer between donor-acceptor emitters

As mentioned earlier, one of the important applications of Green's function is studying the interaction of dipole emitters in the vicinity of nanostructures. For this purpose, a vertical dipole in the vicinity of the graphene-based spherical structure, which was introduced in the previous section, is considered and its Purcell factor is calculated using the Green's function. Assuming that the field point and observation points for the dipole with moment $\mathbf{d}_0^\perp = d_0 \hat{\mathbf{r}}$ are in the same location of $\mathbf{r}' = \Delta > R_1$, $\theta' = 0$, and $\phi' = 0$, by calculating the scattered field using the convolution integral and the use of [18]:

$$\frac{\Gamma_{total}^{d0}}{\Gamma_0} = 1 + \frac{6\pi\epsilon_0}{k_1^3 d_0^2} \text{Im} [\mathbf{d}_0 \cdot \mathbf{E}_{sca}^{d_0}(\mathbf{r}')] \quad (77)$$

where symbol I_m represents the imaginary part of the complex function. The decay rate can be calculated. For this purpose, using relationships:

$$P_n^m(\cos \theta)|_{\theta \rightarrow 0} \simeq \sin^m \theta = \begin{cases} 1 & m = 0 \\ 0 & m \neq 0 \end{cases} \quad (78)$$

$$\frac{dP_n^m(\cos \theta)}{d\theta}|_{\theta \rightarrow 0} \simeq m \sin^{(m-1)} \theta = \begin{cases} 1 & m = 1 \\ 0 & m \neq 1 \end{cases} \quad (79)$$

The scattered field can be calculated. Thus [73]:

$$\frac{\Gamma_{total}^\perp}{\Gamma_0} = 1 - \frac{3}{2} \sum_n n(n+1)(2n+1) \Re \left[\left(\frac{z_n(k_1 \Delta)}{k_1 \Delta} \right)^2 B_V^{11} \right] \quad (80)$$

As can be seen, the above equation is in full agreement with [83] which has extracted the decay rate for a core-shell plasmonic sphere, whereas in this case, it is necessary to use the Mie coefficients of graphene-based structure, namely, B_V^{11} . Using the derived formulas, the positions of the dipole can be considered arbitrarily. The transferred energy between the donor-acceptor pairs can be calculated straightforwardly using the Green's function \mathbf{G} as [84]:

$$\frac{\Gamma(\omega)}{\Gamma_0(\omega)} = \frac{|\mathbf{d}_A \cdot \mathbf{G}(\mathbf{r}_A, \mathbf{r}_B, \omega) \cdot \mathbf{d}_B|^2}{|\mathbf{d}_A \cdot \mathbf{G}_0(\mathbf{r}_A, \mathbf{r}_B, \omega) \cdot \mathbf{d}_B|^2} \quad (81)$$

where the subscript 0 refers to the free-space parameters and \mathbf{d}_A and \mathbf{d}_B are respectively the dipole moments of the acceptor and donor.

4. Conclusion

In conclusion, dyadic Green's function extraction for planarly, cylindrically, and spherically layered medium based on scattering superposition method is a unified

approach to deal with a wide range of electromagnetic problems in the realm of biomedicine. Specifically, the interaction of the human skin, body, and head with the electromagnetic sources with arbitrary distributions can be studied. Moreover, by engineering the constitutive parameters of the layers, a variety of novel devices for medical diagnostics and treatment can be proposed. Plasmonic metals and 2D materials are two main categories of such materials. For the sake of efficient analytical analysis, the impedance boundary condition is satisfied in the case of 2D materials to be used in the design of compact devices.

IntechOpen

IntechOpen

Author details

Shiva Hayati Raad* and Zahra Atlasbaf*
Department of Electrical and Computer Engineering, Tarbiat Modares University,
Tehran, Iran

*Address all correspondence to: shiva.hayati@modares.ac.ir
and atlasbaf@modares.ac.ir

IntechOpen

© 2021 The Author(s). Licensee IntechOpen. This chapter is distributed under the terms of the Creative Commons Attribution License (<http://creativecommons.org/licenses/by/3.0/>), which permits unrestricted use, distribution, and reproduction in any medium, provided the original work is properly cited. 

References

- [1] J. R. Monds and A. G. McDonald, "Determination of skin temperature distribution and heat flux during simulated fires using Green's functions over finite-length scales," *Applied Thermal Engineering*, vol. 50, no. 1, pp. 593–603, 2013.
- [2] J. Schmitt, G. Zhou, E. Walker, and R. Wall, "Multilayer model of photon diffusion in skin," *JOSA A*, vol. 7, no. 11, pp. 2141–2153, 1990.
- [3] A. Christ, T. Samaras, A. Klingenberg, and N. Kuster, "Characterization of the electromagnetic near-field absorption in layered biological tissue in the frequency range from 30 MHz to 6000 MHz," *Physics in Medicine Biology*, vol. 51, no. 19, p. 4951, 2006.
- [4] N. Chahat, M. Zhadobov, L. Le Coq, S. I. Alekseev, and R. Sauleau, "Characterization of the interactions between a 60-GHz antenna and the human body in an off-body scenario," *IEEE Transactions on Antennas Propagation*, vol. 60, no. 12, pp. 5958–5965, 2012.
- [5] S. Caorsi, M. Pastorino, and M. Raffetto, "Analytic SAR computation in a multilayer elliptic cylinder for bioelectromagnetic applications," *Bioelectromagnetics: Journal of the Bioelectromagnetics Society, The Society for Physical Regulation in Biology Medicine, The European Bioelectromagnetics Association*, vol. 20, no. 6, pp. 365–371, 1999.
- [6] K. S. Nikita, G. S. Stamatakos, N. K. Uzunoglu, and A. Karafotias, "Analysis of the interaction between a layered spherical human head model and a finite-length dipole," *IEEE Transactions on Microwave Theory Techniques*, vol. 48, no. 11, pp. 2003–2013, 2000.
- [7] S. Koulouridis and K. S. Nikita, "Study of the coupling between human head and cellular phone helical antennas," *IEEE Transactions on electromagnetic Compatibility*, vol. 46, no. 1, pp. 62–70, 2004.
- [8] J. Kim and Y. Rahmat-Samii, "Implanted antennas inside a human body: Simulations, designs, and characterizations," *IEEE Transactions on microwave theory techniques*, vol. 52, no. 8, pp. 1934–1943, 2004.
- [9] F. Liu and S. Crozier, "Electromagnetic fields inside a lossy, multilayered spherical head phantom excited by MRI coils: models and methods," *Physics in Medicine Biology*, vol. 49, no. 10, p. 1835, 2004.
- [10] F. Keshmiri and C. Craeye, "Moment-method analysis of normal-to-body antennas using a Green's function approach," *IEEE transactions on antennas propagation*, vol. 60, no. 9, pp. 4259–4270, 2012.
- [11] J. S. Meiguni, M. Kamyab, and A. Hosseinbeig, "Theory and experiment of spherical aperture-coupled antennas," *IEEE Transactions on Antennas and Propagation*, vol. 61, no. 5, pp. 2397–2403, 2013.
- [12] H. Khodabakhshi and A. Cheldavi, "Irradiation of a six-layered spherical model of human head in the near field of a half-wave dipole antenna," *IEEE transactions on microwave theory techniques*, vol. 58, no. 3, pp. 680–690, 2010.
- [13] W. C. Chew, *Waves and fields in inhomogeneous media*. IEEE press, 1995.
- [14] J. Sun, C.-F. Wang, J. L.-W. Li, and M.-S. Leong, "Mixed potential spatial domain Green's functions in fast computational form for cylindrically stratified media," *Progress In Electromagnetics Research*, vol. 45, pp. 181–199, 2004.
- [15] T. Itoh, "Spectral domain immittance approach for dispersion characteristics

- of generalized printed transmission lines," *IEEE transactions on Microwave Theory and Techniques*, vol. 28, no. 7, pp. 733–736, 1980.
- [16] M. Thiel and A. Dreher, "Dyadic Green's function of multilayer cylindrical closed and sector-structures for waveguide, microstrip-antenna, and network analysis," *IEEE transactions on microwave theory and techniques*, vol. 50, no. 11, pp. 2576–2579, 2002.
- [17] T. V. B. Giang, M. Thiel, and A. Dreher, "A unified approach to the analysis of radial waveguides, dielectric resonators, and microstrip antennas on spherical multilayer structures," *IEEE transactions on microwave theory and techniques*, vol. 53, no. 1, pp. 404–409, 2005.
- [18] L. Novotny and B. Hecht, *Principles of nano-optics*. Cambridge university press, 2012.
- [19] C. A. Marocico, X. Zhang, and A. L. Bradley, "A theoretical investigation of the influence of gold nanosphere size on the decay and energy transfer rates and efficiencies of quantum emitters," *The Journal of chemical physics*, vol. 144, no. 2, p. 024108, 2016.
- [20] V. Karanikolas, C. A. Marocico, and A. L. Bradley, "Spontaneous emission and energy transfer rates near a coated metallic cylinder," *Physical Review A*, vol. 89, no. 6, p. 063817, 2014.
- [21] K. Rustomji, R. Abdeddaim, C. M. de Sterke, B. Kuhlmey, and S. Enoch, "Measurement and simulation of the polarization-dependent Purcell factor in a microwave fishnet metamaterial," *Physical Review B*, vol. 95, no. 3, p. 035156, 2017.
- [22] A. Vakil, "Transformation optics using graphene: one-atom-thick optical devices based on graphene," 2012.
- [23] C.-T. Tai, *Dyadic Green functions in electromagnetic theory*. Institute of Electrical & Electronics Engineers (IEEE), 1994.
- [24] L.-W. Cai, "On the computation of spherical Bessel functions of complex arguments," *Computer Physics Communications*, vol. 182, no. 3, pp. 663–668, 2011.
- [25] D. Bhattacharya, B. Ghosh, P. K. Goswami, and K. Sarabandi, "Evaluation of Efficient Green's Functions for Spherically Stratified Media," *IEEE Transactions on Antennas and Propagation*, vol. 66, no. 3, pp. 1613–1618, 2018.
- [26] Y. S. Cao, L. J. Jiang, and A. E. Ruehli, "An equivalent circuit model for graphene-based terahertz antenna using the PEEC method," *IEEE Transactions on Antennas and Propagation*, vol. 64, no. 4, pp. 1385–1393, 2016.
- [27] A. Y. Nikitin, F. J. Garcia-Vidal, and L. Martin-Moreno, "Analytical expressions for the electromagnetic dyadic Green's function in graphene and thin layers," *IEEE Journal of Selected Topics in Quantum Electronics*, vol. 19, no. 3, pp. 4600611–4600611, 2012.
- [28] G. W. Hanson, "Dyadic Green's functions and guided surface waves for a surface conductivity model of graphene," *Journal of Applied Physics*, vol. 103, no. 6, p. 064302, 2008.
- [29] G. W. Hanson, "Dyadic Green's functions for an anisotropic, non-local model of biased graphene," *IEEE Transactions on antennas and propagation*, vol. 56, no. 3, pp. 747–757, 2008.
- [30] M. Cuevas, "Surface plasmon enhancement of spontaneous emission in graphene waveguides," *Journal of Optics*, vol. 18, no. 10, p. 105003, 2016.
- [31] T. J. Arruda, R. Bachelard, J. Weiner, and P. W. Courteille, "Tunable Fano resonances in the decay rates of a pointlike emitter near a graphene-coated nanowire," *Physical Review B*, vol. 98, no. 24, p. 245419, 2018.
- [32] E. L. Tan and S. Y. Tan, "A unified representation of the dyadic Green's

functions for planar, cylindrical and spherical multilayered biisotropic media,” *Progress In Electromagnetics Research*, vol. 20, pp. 75–100, 1998

[33] E. L. Tan and S. Y. Tan, “Coordinate-independent dyadic formulation of the dispersion relation for bianisotropic media,” *IEEE Transactions on Antennas Propagation*, vol. 47, no. 12, pp. 1820–1824, 1999.

[34] E. L. Tan and S. Y. Tan, “Concise spectral formalism in the electromagnetics of bianisotropic media,” *Progress In Electromagnetics Research*, vol. 25, pp. 309–331, 2000.

[35] E. Tan, “Vector wave function expansions of dyadic Green's functions for bianisotropic media,” *IEE Proceedings-Microwaves, Antennas propagation*, vol. 149, no. 1, pp. 57–63, 2002.

[36] W.-B. Lu, H. Chen, and Z.-G. Liu, “A review of microwave devices based on CVD-grown graphene with experimental demonstration,” *EPJ Applied Metamaterials*, vol. 6, p. 8, 2019.

[37] J. Zhang, Z. Liu, W. Lu, H. Chen, B. Wu, and Q. Liu, “A low profile tunable microwave absorber based on graphene sandwich structure and high impedance surface,” *International Journal of RF Microwave Computer-Aided Engineering*, vol. 30, no. 2, p. e22022, 2020.

[38] D. Yi, X.-C. Wei, and Y.-L. Xu, “Tunable microwave absorber based on patterned graphene,” *IEEE Transactions on Microwave Theory Techniques*, vol. 65, no. 8, pp. 2819–2826, 2017.

[39] Z. Fang *et al.*, “Active tunable absorption enhancement with graphene nanodisk arrays,” vol. 14, no. 1, pp. 299–304, 2014.

[40] B. Wu *et al.*, “Experimental demonstration of a transparent graphene millimetre wave absorber with

28% fractional bandwidth at 140 GHz,” *Scientific reports*, vol. 4, p. 4130, 2014.

[41] C. Srichan *et al.*, “Highly-sensitive surface-enhanced Raman spectroscopy (SERS)-based chemical sensor using 3D graphene foam decorated with silver nanoparticles as SERS substrate,” *Scientific reports*, vol. 6, p. 23733, 2016.

[42] J. B. Maurya and Y. K. Prajapati, “Experimental Demonstration of DNA Hybridization Using Graphene-Based Plasmonic Sensor Chip,” *Journal of Lightwave Technology*, 2020.

[43] L. A. Falkovsky, “Optical properties of graphene and IV–VI semiconductors,” *Physics-Uspekhi*, vol. 51, no. 9, p. 887, 2008.

[44] H. Nasari and M. Abrishamian, “Nonlinear terahertz frequency conversion via graphene microribbon array,” *Nanotechnology*, vol. 27, no. 30, p. 305202, 2016.

[45] S. Thongrattanasiri, F. H. Koppens, and F. J. G. De Abajo, “Complete optical absorption in periodically patterned graphene,” *Physical review letters*, vol. 108, no. 4, p. 047401, 2012.

[46] S. H. Raad, Z. Atlasbaf, M. Shahabadi, and J. Rashed-Mohassel, “Dyadic Green's Function for the Tensor Surface Conductivity Boundary Condition,” *IEEE Transactions on Magnetics*, vol. 55, no. 11, pp. 1–7, 2019.

[47] Y. R. Padooru, A. B. Yakovlev, C. S. Kaipa, G. W. Hanson, F. Medina, and F. Mesa, “Dual capacitive-inductive nature of periodic graphene patches: Transmission characteristics at low-terahertz frequencies,” *Physical Review B*, vol. 87, no. 11, p. 115401, 2013.

[48] A. Andryieuski and A. V. Lavrinenko, “Graphene metamaterials based tunable terahertz absorber: effective surface conductivity approach,” *Optics express*, vol. 21, no. 7, pp. 9144–9155, 2013.

- [49] Y. Guo, T. Zhang, W.-Y. Yin, and X.-H. Wang, "Improved hybrid FDTD method for studying tunable graphene frequency-selective surfaces (GFSS) for THz-wave applications," *IEEE Transactions on Terahertz Science and Technology*, vol. 5, no. 3, pp. 358–367, 2015.
- [50] J. S. Gomez-Diaz, M. Tymchenko, and A. Alu, "Hyperbolic plasmons and topological transitions over uniaxial metasurfaces," *Physical Review Letters*, vol. 114, no. 23, p. 233901, 2015.
- [51] J. Gomez-Diaz and A. Alu, "Flatland optics with hyperbolic metasurfaces," *ACS Photonics*, vol. 3, no. 12, pp. 2211–2224, 2016.
- [52] A. Fallahi and J. Perruisseau-Carrier, "Design of tunable biperiodic graphene metasurfaces," *Physical Review B*, vol. 86, no. 19, p. 195408, 2012.
- [53] D. L. Sounas and C. Caloz, "Gyrotropy and nonreciprocity of graphene for microwave applications," *IEEE Transactions on Microwave Theory and Techniques*, vol. 60, no. 4, pp. 901–914, 2012.
- [54] L. Lin, L.-S. Wu, W.-Y. Yin, and J.-F. Mao, "Modeling of magnetically biased graphene patch frequency selective surface (FSS)," in *2015 IEEE MTT-S International Microwave Workshop Series on Advanced Materials and Processes for RF and THz Applications (IMWS-AMP)*, 2015, pp. 1–3: IEEE.
- [55] Y. Yermakov *et al.*, "Effective surface conductivity of optical hyperbolic metasurfaces: from far-field characterization to surface wave analysis," *Scientific reports*, vol. 8, no. 1, p. 14135, 2018.
- [56] J. Komijani, J. Rashed-Mohassel, and A. Mirkamali, "Dyadic Green Functions for a Dielectric Layer on a PEMC Plane," *Progress In Electromagnetics Research*, vol. 6, pp. 9–22, 2009.
- [57] J. Gómez-Díaz and J. Perruisseau-Carrier, "Propagation of hybrid transverse magnetic-transverse electric plasmons on magnetically biased graphene sheets," *Journal of Applied Physics*, vol. 112, no. 12, p. 124906, 2012.
- [58] Raad, Shiva Hayati, Zahra Atlasbaf, and Mauro Cuevas. "Dyadic Green's function for the graphene-dielectric stack with arbitrary field and source points." arXiv preprint arXiv: 2104.03581 (2021).
- [59] M. Cuevas, M. A. Riso, and R. A. Depine, "Complex frequencies and field distributions of localized surface plasmon modes in graphene-coated subwavelength wires," *Journal of Quantitative Spectroscopy and Radiative Transfer*, vol. 173, pp. 26–33, 2016.
- [60] M. Hajati and Y. Hajati, "Plasmonic characteristics of two vertically coupled graphene-coated nanowires integrated with substrate," *Applied Optics*, vol. 56, no. 4, pp. 870–875, 2017.
- [61] S. H. Raad and Z. Atlasbaf, "Dyadic analysis of a cylindrical wire consisting of a cover with fully-populated surface conductivity tensor," *Optics express*, vol. 27, no. 15, pp. 21214–21225, 2019.
- [62] J. Gomez-Diaz, M. Tymchenko, and A. Alù, "Hyperbolic metasurfaces: surface plasmons, light-matter interactions, and physical implementation using graphene strips," *Optical Materials Express*, vol. 5, no. 10, pp. 2313–2329, 2015.
- [63] K.-H. Kim, Y.-S. No, S. Chang, J.-H. Choi, and H.-G. Park, "Invisible hyperbolic metamaterial nanotube at visible frequency," *Scientific reports*, vol. 5, p. 16027, 2015.
- [64] Y. Mazor and A. Alù, "Angular-momentum selectivity and asymmetry in highly confined wave propagation along sheath-helical metasurface tubes," *Physical Review B*, vol. 99, no. 15, p. 155425, 2019.

- [65] Y. Huang, Y. Shen, C. Min, and G. Veronis, "Switching photonic nanostructures between cloaking and superscattering regimes using phase-change materials," *Optical Materials Express*, vol. 8, no. 6, pp. 1672–1685, 2018.
- [66] Y. Hua and T. K. Sarkar, "Generalized pencil-of-function method for extracting poles of an EM system from its transient response," 1989.
- [67] C. Tokgoz and G. Dural, "Closed-form Green's functions for cylindrically stratified media," *IEEE Transactions on Microwave theory and Techniques*, vol. 48, no. 1, pp. 40–49, 2000.
- [68] S. H. Raad, C. J. Zapata-Rodríguez, and Z. Atlasbaf, "Multi-frequency super-scattering from sub-wavelength graphene-coated nanotubes," *JOSA B*, vol. 36, no. 8, pp. 2292–2298, 2019.
- [69] S. H. Raad, C. J. Zapata-Rodríguez, and Z. Atlasbaf, "Graphene-coated resonators with frequency-selective super-scattering and super-cloaking," *Journal of Physics D: Applied Physics*, vol. 52, no. 49, p. 495101, 2019.
- [70] S. H. Raad, Z. Atlasbaf, and M. Cuevas, "Scattering from Multilayered Graphene-Based Cylindrical and Spherical Particles," in *Nanoplasmonics*: IntechOpen, 2020.
- [71] X. Ma *et al.*, "Graphene oxide wrapped gold nanoparticles for intracellular Raman imaging and drug delivery," vol. 1, no. 47, pp. 6495–6500, 2013.
- [72] D. Cai, L. Ding, S. Wang, Z. Li, M. Zhu, and H. Wang, "Facile synthesis of ultrathin-shell graphene hollow spheres for high-performance lithium-ion batteries," *Electrochimica Acta*, vol. 139, pp. 96–103, 2014.
- [73] S. H. Raad, Z. Atlasbaf, C. J. Zapata-Rodríguez, M. Shahabadi, and J. Rashed-Mohassel, "Dyadic Green's function for the electrically biased graphene-based multilayered spherical structures," *Journal of Quantitative Spectroscopy Radiative Transfer*, vol. 256, p. 107251, 2020.
- [74] Z.-S. Wu, Z.-J. Li, H. Li, Q.-K. Yuan, and H.-Y. Li, "Off-axis Gaussian beam scattering by an anisotropic coated sphere," *IEEE Transactions on Antennas and Propagation*, vol. 59, no. 12, pp. 4740–4748, 2011.
- [75] L.-W. Li, P.-S. Kooi, M.-S. Leong, and T.-S. Yee, "Electromagnetic dyadic Green's function in spherically multilayered media," *IEEE Transactions on Microwave Theory and Techniques*, vol. 42, no. 12, pp. 2302–2310, 1994.
- [76] M. Farhat, C. Rockstuhl, and H. Bağcı, "A 3D tunable and multi-frequency graphene plasmonic cloak," *Optics express*, vol. 21, no. 10, pp. 12592–12603, 2013.
- [77] F. TING, "Fast solutions of electromagnetic fields in layered media," 2008.
- [78] J. D. Shumpert, "Modeling of Periodic Dielectric Structures (electromagnetic Crystals)," University of Michigan, 2001.
- [79] M. Wan *et al.*, "Strong tunable absorption enhancement in graphene using dielectric-metal core-shell resonators," *Scientific reports*, vol. 7, no. 1, p. 32, 2017.
- [80] S. H. Raad, Z. Atlasbaf, J. Rashed-Mohassel, and M. Shahabadi, "Scattering from graphene-based multilayered spherical structures," *IEEE Transactions on Nanotechnology*, vol. 18, pp. 1129–1136, 2019.
- [81] S. H. Raad and Z. Atlasbaf, "Equivalent RLC ladder circuit for scattering by graphene-coated nanospheres," *IEEE Transactions on Nanotechnology*, vol. 18, pp. 212–219, 2019.
- [82] S. H. Raad and Z. Atlasbaf, "Tunable optical meta-surface using graphene-

coated spherical nanoparticles,” *AIP Advances*, vol. 9, no. 7, p. 075224, 2019.

[83] T. J. Arruda, A. S. Martinez, F. A. Pinheiro, R. Bachelard, S. Slama, and P. W. Courteille, “Fano resonances in plasmonic core-shell particles and the Purcell effect,” in *Fano Resonances in Optics and Microwaves*: Springer, 2018, pp. 445–472.

[84] V. D. Karanikolas and A. L. Bradley, “Interactions Between Quantum Emitters in the Presence of Plasmonic Nanostructures,” Trinity College Dublin, 2016.

IntechOpen